FOI-R--0700--SE
December 2002
ISSN 1650-1942
Technical report

Lars Sjöqvist, Ove Steinvall

Aero-optical and plume effects in airborne laser countermeasure applications

SWEDISH DEFENCE RESEARCH AGENCY

Sensor Technology
P.O. Box 1165
SE-581 11 Linköping

FOI-R--0700--SE

December 2002

ISSN 1650-1942

Technical report

Lars Sjöqvist, Ove Steinvall

Aero-optical and plume effects in airborne laser countermeasure applications

Issuing organization
FOI – Swedish Defence Research Agency
Sensor Technology
P.O. Box 1165
SE-581 11 Linköping

Report number, ISRN
FOI-R--0700--SE

Report type
Technical report

Research area code
6. Electronic Warfare

Month year
December 2002

Project no.
E3020

Customers code
5. Commissioned Research

Sub area code
61 Electronic Warfare including Electromagnetic Weapons and Protection

Author/s (editor/s)
Lars Sjöqvist
Ove Steinvall

Project manager
Ove Steinvall

Approved by
Svante Ödman

Sponsoring agency
The Swedish Headquarter

Scientifically and technically responsible
Lars Sjöqvist

Report title
Aero-optical and plume effects in airborne laser countermeasure applications

Abstract (not more than 200 words)
In airborne laser countermeasure applications (DIRCM) several sources of perturbations, which affect the performance of the system, need to be considered. The main task of a DIRCM system is to optimise the laser irradiance at the target (missile) for a certain time until break-lock can be verified. Perturbations such as; platform-induced jitter, aero-optical effects, jet engine exhaust plumes and strong turbulence may severely degrade the performance.

In this report strong perturbations relevant for DIRCM applications have been reviewed. The most important aero-optical effects include turbulent boundary and shear layers, inviscid flow and shocks. Contributions from these effects to the laser beam quality have been estimated using simple models and experimental data. Experimental data and models available on plume effects, relevant for fast jet installations, have been reviewed. Calculations aiming to estimate the tracking performance and beam optimisation in different turbulence situations are presented.

Keywords
Aero-optics, plume, turbulence, DIRCM, laser, beam propagation

Further bibliographic information

Language English

ISSN 1650-1942

Pages 58 p.

Price acc. to pricelist

Utgivare
Totalförsvarets Forskningsinstitut - FOI
Sensorteknik
Box 1165
581 11 Linköping

Rapportnummer, ISRN
FOI-R--0700--SE

Klassificering
Teknisk rapport

Forskningsområde
6. Telekrig

Månad, år
December 2002

Projektnummer
E3020

Verksamhetsgren
5. Uppdragsfinansierad verksamhet

Delområde
61 Telekrigföring med EM-vapen och skydd

Författare/redaktör
Lars Sjöqvist
Ove Steinvall

Projektledare
Ove Steinvall

Godkänd av
Svante Ödman

Uppdragsgivare/kundbeteckning
HKV

Tekniskt och/eller vetenskapligt ansvarig
Lars Sjöqvist

Rapportens titel (i översättning)
Aero-optiska och plymeffekter vid flygburna lasermotmedelstillämpningar

Sammanfattning (högst 200 ord)
I flygburna laserbaserade motmedelstillämpningar (DIRCM) måste flera störningskällor som påverkar systemprestanda beaktas. Huvudsyftet med ett DIRCM-system är att optimera intensiteten från lasern på målet (robot) under en viss tid tills verkansverifiering kan bekräftas. Störningar som plattformsvibrationer, aero-optiska effekter, plymer från jetmotorer och kraftig turbulens kan allvarligt försämra systemprestanda.

I den här rapporten har kraftiga störningar som är relevanta för prestanda hos ett DIRCM-system undersökts. De viktigaste aero-optiska effekterna inkluderar turbulenta skikt som uppstår kring plattformen, kompressibla luftströmmar och shockfenomen. Bidrag från dessa fenomen till laserstrålens kvalité har uppskattats med enkla modeller och experimentella data. Experimentella resultat och modeller för avgasplymer, relevanta för tillämpningar som inkluderar snabba jetflygplan, har studerats. Beräkningar för att uppskatta följningsnoggrannhet och stråloptimering i olika turbulenssituationer presenteras i rapporten.

Nyckelord
Aero-optik, avgasplym, turbulens, dircm, laser, strålutbredning

Övriga bibliografiska uppgifter

Språk Engelska

ISSN 1650-1942

Antal sidor: 58 s.

Distribution enligt missiv

Pris: Enligt prislista

CONTENT

1. INTRODUCTION

Laser countermeasures, or Directed Infrared Countermeasures (DIRCM), have been developed to protect advanced technological airborne platforms from infrared (IR) guided missile threats. The threats from shoulder-fired surface-to-air (SAM), vehicle mounted surface-to-air and air-to-air (AA) missiles are increasing. The traditional methods of self-protection i.e. using pyrotechnic flares and decoys are believed to be insufficient for the next generation of IR-guided missiles. Therefore, DIRCM-systems are currently developed for self-protection of large transport aircrafts, helicopters and fast jet (FJ) fighters. The DIRCM system utilises a laser beam to obtain sufficient brightness in front of the threat missile causing efficient jamming due to a high jammer to signal (target) ratio. Since the laser beam has a small lobe and is highly directional a large amount of the emitted radiation can be used to jam the threat missile. The critical components of a DIRCM system is the laser transmitter, designed to deliver high power in the wavelength region where the seeker operates, and the acquisition, pointing and tracking system (APT) which is responsible for pointing the laser beam to the correct position and track the target. A schematic description of a DIRCM system is depicted in Figure 1. The first event in the DIRCM chain (1) is the detection of the threat missile by the missile approach warning system (MAWS), secondly the APT starts to track the missile (2) and in the final step is the laser switched on using an appropriate jamming code to cause the break-lock of the missile (3).

The performance of the DIRCM system is dependent on several external sources of perturbations. Mechanical jitter on the platform reduces the averaged power in front of the missile aperture. Aero-optical effects and perturbations due to the exhaust plume from the engine are other contributions, which can degrade the performance of the DIRCM system due to induced aberrations in the laser beam.

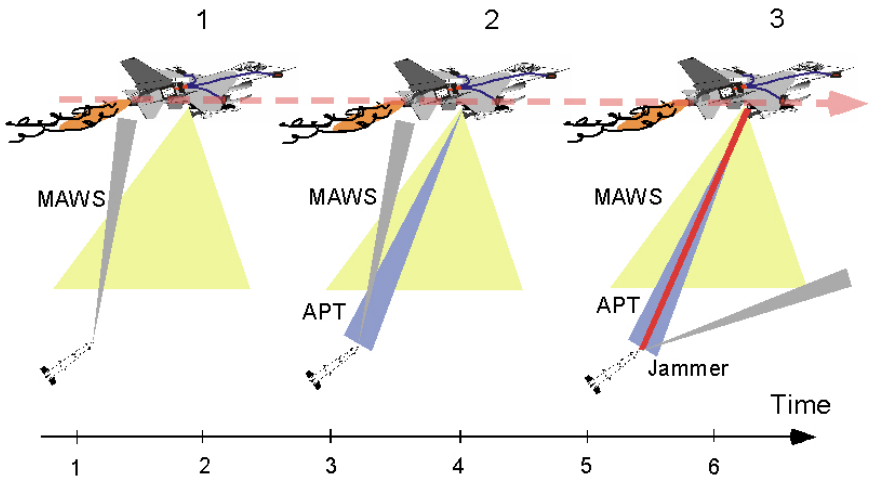

Figure 1 Schematic description of the basic functions in a DIRCM system. MAWS: missile approach warning (yellow) system, APT: acquisition, pointing and tracking unit (blue), Jammer: laser transmitter (red). The missile field of view is indicated in grey.

Extreme environments are present considering a DIRCM application on a fast jet platform (Figure 2). In certain scenarios the APT (acquisition, pointing and tracking) system needs to be able to direct the beam close to, or partly through, the jet engine plume. Propagation of a laser beam in close vicinity to the exhaust may induce severe degradation of the laser beam quality. Although the spatial extent of the plume

is limited, in comparison to the total propagation distance, the distortions of the beam passing through a region with strongly fluctuating refractive index are accumulated. Effects observed due to the perturbations include beam broadening, intensity scintillations and wandering of the beam centroid. The perturbations originating from the jet engine exhaust can be several orders of magnitude larger than turbulence effects experienced under normal atmospheric conditions.

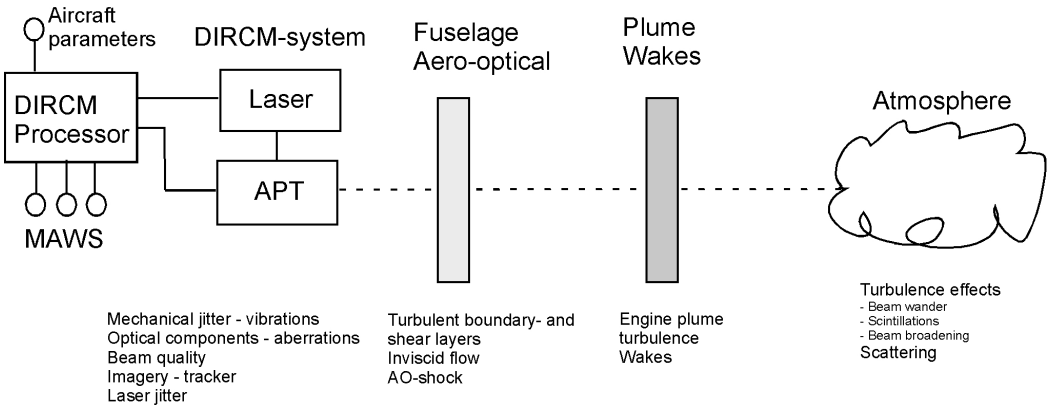

Figure 2 Factors affecting the performance of a DIRCM system situated on a fast jet platform.

Turbulence effects affecting the quality of the laser beam related to the engine exhaust depend on several parameters. The extent of the turbulence profile (both transversal and longitudinal), described in terms of the structure parameter, needs to be known as a function of time in order to estimate the averaged effect of the plume. The structure parameter can be used to describe the alterations in refractive index during passage through the plume. Important parameters related to the flowing gases affecting the local turbulence are the transversal and axial velocities, temperature variations and temperature gradients. Local zones of strong turbulence are characteristic features of the exhaust plume. A structure parameter, C_n^2, in the region 10^{-9} to 10^{-10} $m^{-2/3}$ can be anticipated within the plume. The inner- and outer scale of the turbulence, which describe the size of the smallest and largest Eddies, are in the sub-mm and sub-meter range, respectively. Hence, high spatial frequency content can be expected from the spectrum describing intensity variations during propagating through exhaust plumes. The geometric aspects during propagation in vicinity, or through, the plume is of importance since the plume is anisotropic from an optical point of view. The flow characteristics vary along the flow axis, exhibiting nearly laminar jet flow close to the exhaust, an intermediate mixing region and a plume with fully developed turbulence. Considering temporal fluctuations of the refractive index the laser beam diameter, transversal velocity and the coherence length of the perturbations are relevant for bandwidth estimations.

Another source of aberration is aero-optical effects occurring due to the movement of the platform in air. For example, the fuselage of the aircraft introduces turbulent boundary- and shear layers that affect the optical field (both the outgoing laser beam and the incoming image). Other effects due to air motion are inviscid flow and shocks. Several parameters have an effect on the influence from aero-optical phenomena on laser beam propagation such as location of the APT on the platform, the velocity of the platform, altitude, wavelength of the radiation, geometrical aspects of the APT etc. These parameters need to be considered in developing a DIRCM system. The platform influence is crucial in the case of a fast jet installation because of the high velocity and the external forces. The optical effects originating from AO-phenomena include beam broadening and wander which reduce the brightness in front of the seeker aperture.

In this report results from experimental studies of laser beam propagation effects observed in jet engine exhaust and rocket engine plumes performed at FOI and Saab Bofors/Saab Avionics (former Bofors Missiles/Celsius Tech Electronics) and literature results are reviewed. A short survey covering theoretical models and methods of laser beam propagation through strong turbulence is presented. Tracking and power bucket calculations have been performed to investigate the performance of the APT in strong turbulence situations. The influence of aero-optical effects in a DIRCM application is evaluated. The consequences of turbulence effects in the engine exhaust and AO-phenomena are analyzed in conjunction to the DIRCM application.

2. ATMOSPHERIC TURBULENCE

Atmospheric turbulence may impact the performance of a laser countermeasure application dramatically. The origin of optical turbulence is temporal and spatial variations in the index of refraction, $n(\underline{r},t)$, due to temperature and pressure fluctuation of the air. These variations cause optical effects such as:

- Beam broadening
- Beam wander
- Intensity scintillations
- Angle of arrival fluctuations.

All these effects may degrade the performance of a DIRCM system, and need consequently to be carefully analysed. The strength of the turbulence is expressed in terms of the structure parameter, C_n^2. Several models for the structure parameter have been developed and experimental data are available for different conditions [2]. The structure parameter varies from, $C_n^2 \approx 10^{-13} - 10^{-17}$ m$^{-2/3}$ in the atmosphere, where the larger value corresponds to the turbulence strength close to ground and the smaller value to an altitude of approximately 10 km, respectively. The turbulence strength can be categorized as follows for atmospheric conditions; weak turbulence $C_n^2 \sim 10^{-17} - 10^{-16}$, moderate turbulence $C_n^2 \sim 10^{-15} - 10^{-14}$ and strong turbulence $C_n^2 \sim 10^{-13} - 10^{-12}$ m$^{-2/3}$. In extreme turbulence conditions values of C_n^2 of the order $10^{-10} - 10^{-9}$ m$^{-2/3}$ can be observed. Using information how the structure parameters vary along a propagation path beam properties can be calculated. An example of C_n^2 variations as a function of the altitude is shown in Figure 3 using the Hufnagel-Valley model. Depending on the local conditions an appropriate model can be chosen for atmospheric turbulence effect at higher altitude. Close to ground the situation becomes more complicated and the beam can be severely degraded for longer horizontal propagation paths close to ground.

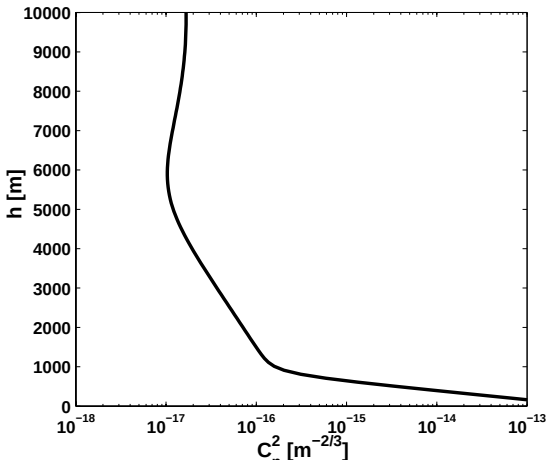

Figure 3 Variation of the structure parameter, C_n^2, as a function of altitude (h) using the Hufnagel-Valley model [1] with $A = 5 \cdot 10^{-13}$ $m^{-2/3}$ and v = 21 m/s.

In a DIRCM application (fast jet) the strong turbulence effects originating from natural atmospheric conditions can often be neglected except for the situation when the FJ is close to ground (i.e. $h \sim$ 100-200 m) and the beam path is nearly horizontal. This situation may occur if a SAM missile is fired when the FJ is taking off or preparing for landing. At higher altitudes only the last part of the beam path is influenced by the stronger turbulence close to ground, which reduces the degradation effects considerably.

One characteristic feature of laser beam propagation in strong turbulence is the appearance of scintillation effects i.e. beam spatial and temporal beam intensity fluctuations. The scintillation phenomenon causes spatial beam break-up and movements of air masses due to winds cause a temporal fluctuation of the scintillation. The scintillation effect in weak (to moderate) turbulence strength can be estimated using the following expressions for the variance of the intensity

$$\sigma_I^2 = 2.24k^{\frac{7}{6}} \int_0^L C_n^2(z)(L-z)^{\frac{5}{6}}\, dz \quad (\textit{plane wave}) \qquad \text{eq. 1}$$

And

$$\sigma_I^2 = 2.24k^{\frac{7}{6}} \int_0^L C_n^2(z)\left(\frac{z}{L}\right)^{\frac{5}{6}}(L-z)^{\frac{5}{6}}\, dz \quad (\textit{spherical wave}) \qquad \text{eq. 2}$$

where $k = 2\pi/\lambda$ and L is the propagation distance. One condition for eq. 1 and eq. 2 to be fulfilled is that $l_o \ll \sqrt{\lambda L}$ where l_o is the inner scale length of the turbulence.

2.1 Models describing laser beam propagation in strong turbulence conditions

Propagation of laser beams through weak turbulence has been described thoroughly in the literature [2]. Analytical expressions for relevant turbulence parameters such as the intensity distribution, beam wandering and beam broadening have been derived. Usually Rytov theory is satisfactory to describe phenomena appearing in the weak turbulence regime. In the case of strong turbulence conditions the

situation becomes more complicated. Closed analytical solutions describing the statistical behaviour of the refractive index fluctuations due to strong turbulence effects are cumbersome or not possible to derive. Only asymptotic solutions with limited regions of validity are viable. The most common approach to study effects in the strong fluctuation and saturation regime is to use numerical methods.

Several models describing the power spectral density of refractive index variations in the atmosphere have been proposed. The most commonly used model, valid in the inertial sub-range ($L_o^{-1} << \kappa << l_o^{-1}$), is the Kolmogorov spectrum

$$\Phi(\kappa) = 0.033 C_n^2 \kappa^{-\frac{11}{3}} \qquad \text{eq. 3}$$

where κ is the spatial frequency. One drawback with the Kolmogorov spectrum is the limited validity at high and low spatial frequencies. The effect of inner- and outer scales, l_o and L_o, can be included by considering the modified von Karman spectrum

$$\Phi(\kappa) = 0.033 C_n^2 \frac{\exp(\frac{\kappa}{\kappa_m})^2}{(\kappa^2 + \kappa_o^2)^{\frac{11}{6}}} \qquad \text{eq. 4}$$

with $\kappa_m = (2\pi/L_o)$ and $\kappa_o = (5.92/l_o)$. An example showing inner- and outer scale effects is depicted in Figure 4. A reduction in the normalised power spectral density is observed using the von Karman spectrum at low spatial frequencies due to a small outer scale. At higher frequencies, on the other hand, the von Karman spectrum is close to the Kolmogorov predictions. An alternative spectrum was proposed to describe laser beam propagation through zones of strong turbulence by Vorobev and co-workers [3]. In their description the finite effects of the inner- and outer scale are taken into account. This spectrum was adapted to experimental data and a model describing laser beam propagation through zones of strong turbulence using the phase screen method was presented. Using the modified spectrum agreement between the experimental observations and simulated data were obtained.

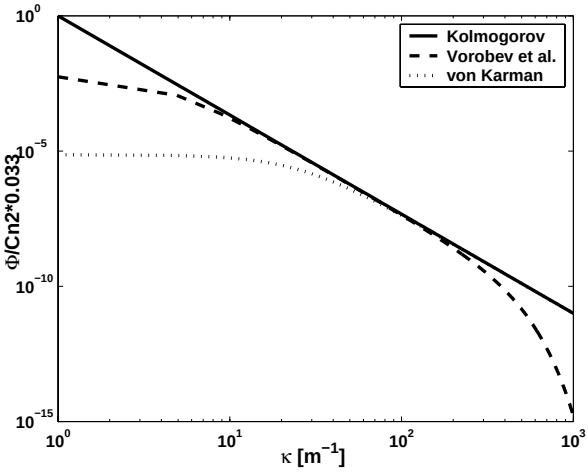

Figure 4 Variation in normalised spectral density as a function of spatial frequency for the Kolmogorov, von Karman and Vorobev et al.[3] spectral functions. The following inner and outer scales were used: L_o = 0.25 m and l_o = 0.5 mm.

In order to predict small- and large-scale turbulence effects the von Karman or the spectrum proposed by Vorobev et al. can be used as a first approximation. The spectrum of the refractive index variations is required utilising the phase screen method for laser beam propagation in turbulence conditions (see below).

2.1.1. Beam wander

The beam wander can be divided into two different time scales describing short- and long term broadening of the laser beam [4,5]. The characteristic time constant for the motion of the beam centroid depends on $\tau = D/v$, where D is the beam diameter and v the transversal velocity. The short term broadening of the beam originates from small turbulence cells with high spatial frequency. The long-term mean square beam radius $\langle \rho_L^2 \rangle$ can be expressed as (assuming an exposure time $t >> \tau$) [4]:

$$\langle \rho_L^2 \rangle = \langle \rho_S^2 \rangle + \langle \rho_c^2 \rangle \qquad \text{eq. 5}$$

where ρ_s is the short term beam broadening and ρ_c defines the motion of the beam centroid, respectively. It should be noted that the expression given above is only valid in the presence of weak (moderate) turbulence. Assuming a gaussian beam shape the long-term beam radius can be written as

$$\langle \rho_L^2 \rangle \cong \frac{4z^2}{k^2 D} + \frac{D^2}{4}\left(1 - \frac{z}{F}\right)^2 + \frac{4z^2}{k^2 \rho_o^2} \qquad \text{eq. 6}$$

where the transversal coherence length is defined as

$$\rho_o = \left[1.46 k^2 z \int_0^1 (1-\xi)^{\frac{5}{3}} C_n^2(\xi z)\, d\xi\right]^{-\frac{3}{5}} \qquad \text{eq. 7}$$

and z the propagation distance, D the beam diameter and F the phase radius. The condition $z << \left(k^2 C_n^2 l_o^{\frac{5}{3}}\right)^{-1}$ needs to be fulfilled for eq. 6 to be valid. If $z >> \left(k^2 C_n^2 l_o^{\frac{5}{3}}\right)^{-1}$ then the long term beam radius can be written as

$$\langle \rho_L^2 \rangle \cong \frac{4z^2}{k^2 D} + \frac{D^2}{4}\left(1 - \frac{z}{F}\right)^2 + \frac{6.6 z^3 \int_0^1 (1-\xi^2) C_n^2(\xi z) d\xi}{l_o^{\frac{1}{3}}}. \qquad \text{eq. 8}$$

Studying the short term beam broadening and the centroid motion four different cases can be identified. If $\rho_o << D < L_o$ *and* $z \le kL^2$ then

$$\left\langle \rho_S^2 \right\rangle = \frac{4z^2}{k^2 D^2} + \frac{D^2}{4}\left(1-\frac{z}{F}\right)^2 + \frac{4z^2}{k^2\rho_o^2}\left[1-0.62\left(\frac{\rho_o}{D}\right)^{\frac{1}{3}}\right]^{\frac{6}{5}}$$

$$\left\langle \rho_C^2 \right\rangle = \frac{2.97 z^2}{k^2 \rho_o^{\frac{5}{3}} D^{\frac{1}{3}}} \qquad \text{eq. 9}$$

where L is defined as min[ρ_o,D]. The second case belong to the situation when $\rho_o \approx D$ *and* $z \le kL^2$ and in this case analytical solutions to the centroid motion and short-term beam wander can not be found (see ref.[4] for numerical solutions). If the transversal coherence radius is much larger than the beam diameter i.e. $\rho_o >> D$ *and* $z \le kL^2$, the effects from short and long term beam wander are approximately equal implying that eq. 6 can be used. Close to saturation when $z \le kL^2$ the centroid beam wander can be neglected in comparison to the long term broadening. In this case

$$\frac{\left\langle \rho_C^2 \right\rangle}{\left\langle \rho_L^2 \right\rangle} \approx \left(\frac{k\rho_o^2}{z}\right)^{\frac{1}{3}} \qquad \text{eq. 10}$$

which means that $\rho_L^2 >> \rho_C^2$ if the range z is large.

Beam wander has also been described using geometrical optics [6]. The variance of the beam wander could in this case be expressed as

$$\sigma^2 = 2.92 D^{-\frac{1}{3}} L^3 \int_0^1 C_n^2(x) \frac{(1-x)^2}{\left|1-\frac{L}{F}x\right|^{\frac{1}{3}}} dx \qquad \text{eq. 11}$$

where the integration variable is $x = z_1/L$. This expression is valid within 5% under the assumption $\sqrt{\lambda L} \le D << L_o$. A more accurate expression for the beam wander was derived by Klyatskin and Kon using the Markov approximation [7]

$$\sigma^2 = 4\pi^2 \int_0^L (L-z)^2 dz \int_0^\infty \Phi_n(k,z) K^3 dK \times e^{\left\{-\frac{K^2D^2}{8}\left[(1-\frac{z}{F})^2+\frac{16z^2}{k^2D^4}\right]-\pi D(Kz/k)\right\}} \qquad \text{eq. 12}$$

where $\Phi_n(k,z)$ is the spectrum for the refractive index fluctuations and the structure function

$$D(\rho) = 8\pi^2 k^2 \int_0^z dz' \int_0^\infty dK' K' \Phi(K', z')\left[1 - J_o(K'\rho z'/z)\right] \qquad \text{eq. 13}$$

where J_o is the zero-order Bessel function. Due to the complicated form of eq. 12 the beam wander can to first order be estimated using the simplified expression described above and within the given validity ranges the deviation from the exact formula is small.

Recently, Sirazetdinov and co-workers have studied the effects of laser beam propagation through a jet engine exhaust [8,9]. The beam broadening and beam wander were studied at different aspect angles relative the symmetry axis of the exhaust (0, 45 and 90^o) using a sophisticated experimental set-up. Anisotropic effects during propagation through the jet engine exhaust were observed for the beam broadening and the motion of the beam centroid. The asymmetric beam broadening resulted in an

elliptical shaped beam profile with the long axis directed perpendicular to the flow axis. An analytical model was used to compare the beam broadening and wandering which agreed with the experimental results. The variance of the beam centroid wander was modelled using the following expression for the variance of the beam centroid

$$\sigma_i^2(a) = 2.84 C_n^2 L_t (2a)^{-\frac{1}{3}} \left\{ 1 - 0.1 \left[\frac{4a^2}{L_{oi} L_{oj}} \right]^{\frac{1}{6}} \left[3 \left(\frac{L_{oi}}{L_{oj}} \right)^2 + 1 \right] \right\} \qquad \text{eq. 14}$$

where $L_{oi,j}$ is the outer scale factors, a is the beam radius, L_t the propagation distance and $i,j = x$ or y coordinate, respectively. The anisotropic behaviour of the beam centroid motion is taken into account using eq. 14. The structure function used in the study included the presence of anisotropy. The utilised model is valid if the beam size is smaller than the outer scale factors i.e. $a << L_{oi,j}$. According to eq. 14 the beam centroid motion is not dependent on the transversal coherence radius. A spectrum model, based on the von Karman spectrum, but modified to include high spatial frequency components and the anisotropy (see above) was suggested for calculation of the centroid motion. Stronger wavelength dependence for the beam broadening than predicted by conventional theory was reported.

The magnitudes of beam wander beam wander expected for a collimated beam and different beam size and atmospheric parameters are depicted in Figure 5. Increasing the turbulence strength from $C_n^2 = 10^{-16}$ to 10^{-13} $m^{-2/3}$ causes a dramatic increase in the rms beam wander. The values shown for the beam wander in Figure 5 corresponds to rather long horizontal propagation distances (3 to 10 km). One important observation from the formulas presented above is the fact that the centroid beam wander is independent of the wavelength. The size of the beam diameter has a small effect on the beam wander as illustrated in Figure 5B.

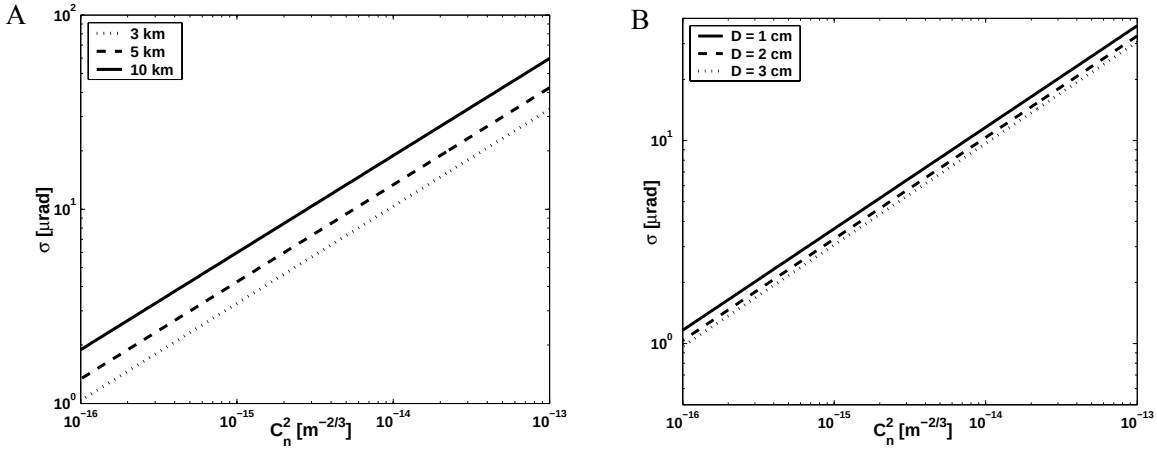

Figure 5 A) RMS beam wander as a function of the C_n^2 for different propagation distances in atmospheric turbulence (beam diameter $2w_o = 2$ cm) B) RMS beam wander as a function of the C_n^2 for propagation through turbulent atmosphere a distance L = 3 km and varying the size of the beam diameter.

Considering the magnitudes of the beam wander due to atmospheric turbulence the mechanically induced platform jitter most likely give the largest contribution to the total beam deflection at high altitudes neglecting AO-effects and influence from the plume.

2.1.2. Phase screen methods

The method of successive phase screens has been utilised to study beam properties under small-scale turbulence conditions and to study outer scale effects on beam centroid motion [10,11]. A numerical method scheme based on Monte-Carlo simulations and the parabolic wave equation was used to calculate beam wander and broadening due to turbulence. This method has been used to interpret beam degradation effects observed during laser beam propagation in a jet engine exhaust [12]. It was shown that the numerical model agreed satisfactorily with experimental results at λ = 1.06 and 10.6 μm, respectively. The results indicated that the model could be used to simulate turbulence strengths in the range, $C_n^2 = 10^{-9}$-10^{-11} $m^{-2/3}$.

A simple numerical propagation model has been developed in this work to simulate tracking and pointing capabilities in laser countermeasure applications. The method utilises the method of successive phase screens to represents different perturbations experienced by the laser beam. In a first step perturbations originating from mechanical jitter and turbulence effects have been included in the model. The model is based on physical optics whereas the optical field is propagated using the Fresnel operator formalism and FFT (angular spectrum). The model employs the GLAD calculation engine for propagation of the optical field [13]. In this type of calculations the optical field *a(x,y)* can be written a

$$a'(x,y) = a(x,y)e^{ikW(x,y)} \qquad \text{eq. 15}$$

where *W(x,y)* represents different sources of phase aberrations. The mechanical induced jitter, e.g. in a APT beam director, can be described by an ordinary Seidel polynomial

$$W(r,\theta) = W_{11}(\frac{r}{r_{norm}})\cos(\theta - \theta_o) \qquad \text{eq. 16}$$

where r and θ are polar coordinates and r_{norm} a normalisation factor. By treating r and θ as random variables the jitter contribution due to tilt (and azimuth) can be calculated. In the model the jitter component is specified as a rms value in terms of the wavelength. An example of a tilted phase distribution representing tilt jitter is depicted in Figure 6A. The result, which can be obtained from the model, is exemplified by studying the beam motion (centroid) at a target board for a typical laser countermeasure scenario. A Gaussian beam was assumed to be diffraction limited having a 1 cm radius, wavelength λ = 4.0 μm, range z = 3 km and the rms jitter was 50 μrad. The motion of the beam centroid due to the jitter is shown in Figure 6B.

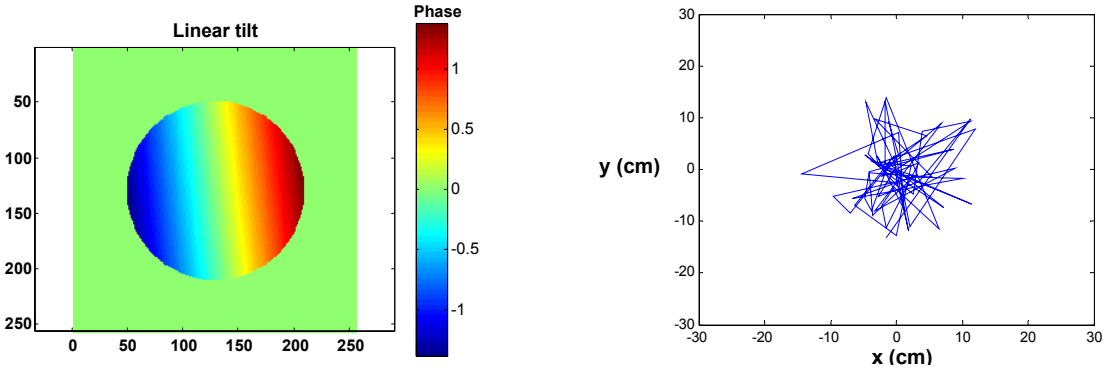

Figure 6 A) Linear phase distribution across the beam profile representing the effects of mechanical jitter. B) Calculated centroid motion at z = 3 km range due to mechanical jitter. The line represents the motion of the beam centroid on a target board.

Atmospheric turbulence has also been incorporated in the model assuming a modified Kolmogorov spectral distribution. This spectrum contains both the inner- and outer scale factors as parameters and is defined according to

$$\Phi^2(\kappa) = 0.023 \cdot \frac{e^{-l_o^2 \kappa^2}}{r_o^{\frac{5}{3}} (\kappa^2 + L_o^{-2})^{\frac{11}{6}}} \qquad \text{eq. 17}$$

where k is the spatial frequency, l_o and L_o the inner- and outer scale, respectively. The Fried parameter, r_o, defines the strength of the turbulence. An example illustrating presence of both mechanical jitter and turbulence is shown in Figure 7. Typical beam break-up can be observed due to the atmospheric turbulence. The instantaneous peak irradiance varies considerably due to the jitter and turbulence effects. Hence, adaptive feedback is required to control a tip-tilt mirror which purpose is to reduce the influence of the jitter. The developed model does not contain any temporal information in the present version. However, temporal information can be incorporated if the frequency behaviour of the jitter and turbulence is known. Further improvements of the model include; closing the loop by adding feedback and a tracking detector, compensation elements and improved phase screen generators which take better account of the large scale motion i.e. the beam centroid. Another important task is to validate the model by comparing simulated and experimental data. The model can, in the present version, carry out simulations predicting effects from jitter and turbulence in more complex laser countermeasure applications.

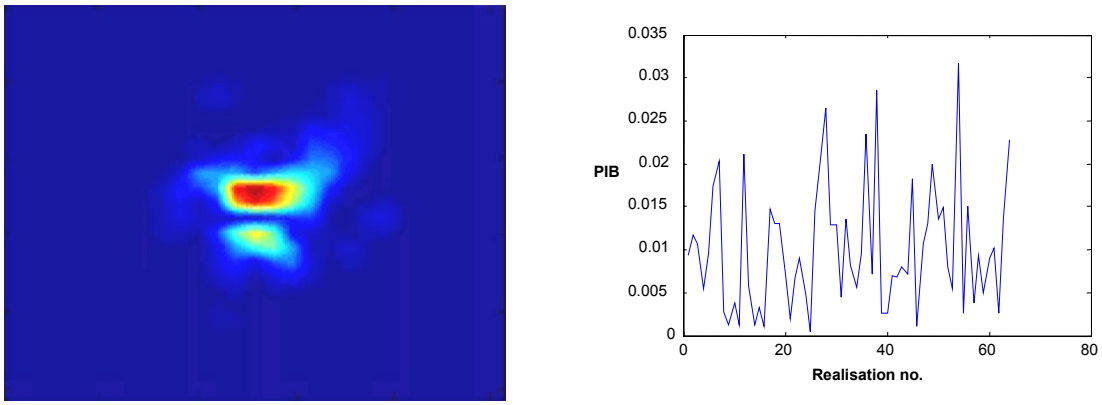

Figure 7 A) Beam profile at the target plane, range z = 3 km. B) Power in bucket (PIB) variations due to jitter and atmospheric effects in the target plane at range z = 3 km. The atmospheric parameters were; l_o = 1 mm, L_o = 10 m and r_o = 1 cm. The diameter used for power in bucket calculations was D = 10 cm.

2.1.3. Scintillation effects

Extensive expressions for scintillation effects due to laser beam propagation in a turbulent atmosphere have been presented recently [2,14]. Andrews and Phillips cover the scintillation phenomena both in the weak, medium and strong turbulence regions.

2.1.4. Condition for saturation

One interesting question, which arises, is whether a laser beam saturates during propagation through an engine plume and the conditions to be fulfilled to avoid saturation. One common method to decide whether an optical wave is saturated or not, is to compare the Fresnel scale with the spatial coherence length i.e.

$$\rho_o > \sqrt{\frac{L}{k}} \qquad \text{eq. 18}$$

where ρ_o is the spatial coherence length and $\sqrt{\frac{L}{k}}$ is the Fresnel scale. As long as the condition in eq. 18 is fulfilled the scintillation can be considered non-saturated. By calculating the coherence length during propagation through a plume the effect of saturation can be estimated to first order. Another condition for saturation (observed experimentally) is defined as $\sigma_{\ln I}^2 \approx 2$, where $\sigma_{\ln I}^2$ is the log-irradiance variance.

One effect excluded in this discussion is related to the fact that the radiation may pass through the same path twice if the retro reflex phenomenon is utilised for tracking. Double-passage effects give rise to enhanced backscatter, which may increase the on-axis irradiance in the receiver plane due to constructive interference between different parts of the beam. The double-passage phenomena have been discussed by Andrew and Phillips[2]. Fade characteristic have been estimated for another application involving laser communication, but the expressions derived should be applicable to the DIRCM scenario in order to estimate characteristics of the retro reflex signal and tracking performance [15].

3. TRACKING IN STRONG TURBULENCE

Using signal statistics and probability density functions simulations of the performance of a DIRCM system can be carried out. In this method beam perturbations such as mechanical induced jitter and turbulence effects are treated from a statistical point of view. It is of interest to compare different situations whereas the magnitudes of the perturbations vary e.g. weak atmospheric turbulence occurring at high altitude in comparison to a low altitude scenario whereas stronger turbulence can be anticipated. An even more demanding case occurs if a perturbation contribution from the jet engine plume needs to be included. In paragraph "7 Appendix – Tracking optimisation using signal statistics" calculations studying detection characteristics of a DIRCM system in the cases of high and low signal levels are presented. The power in bucket (PIB) i.e. the irradiance in front of the missile aperture is a suitable figure of merit for characterizing the performance in DIRCM. The PIB was investigated in presence of beam jitter and strong turbulence. Another important subject is the best achievable tracking accuracy in presence of perturbations. The tracking accuracy is associated to the beam dimensions since a narrow laser beam requires a higher tracking accuracy to reduce signal fading.

One important parameter used throughout the calculations is optimum beam size parameter, α, defined as

$$\alpha = \frac{w}{\sigma_j} \qquad \text{eq. 19}$$

where w is the beam radius and σ_j the standard deviation of the laser beam jitter. Another definition, which occasionally used is $\beta = \alpha^2$.

An example showing how the detection probability, *Pd*, depends on the signal to noise ratio (SNR) is illustrated in Figure 8. The detection probability decreases considerably in presence of strong turbulence as indicated in comparison to vacuum propagation. In this calculation was the strong turbulence represented by an exponential probability density function (PDF) [14]. The influence of the beam parameter β with respect to the total detection probability is not so pronounced in presence of strong turbulence. Varying β from 1.5 to 10 caused only a minor change in the detection probability.

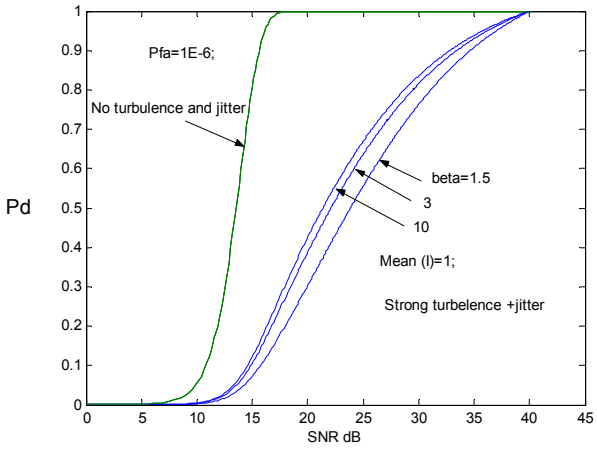

Figure 8. Total detection probability vs. SNR for different $\beta = \alpha^2$ during strong turbulence and jitter. Pfa denotes the false alarm rate.

The PIB calculations show that an optimum beam parameter exists in presence of weak to moderate turbulence (Figure 9). If the maximum intensity is calculated as a function of the beam parameter a characteristic max exist for different turbulence and jitter magnitudes. In the presence of strong turbulence, on the other hand, no maximum can be observed since the relative influence of a is reduced (see appendix 7).

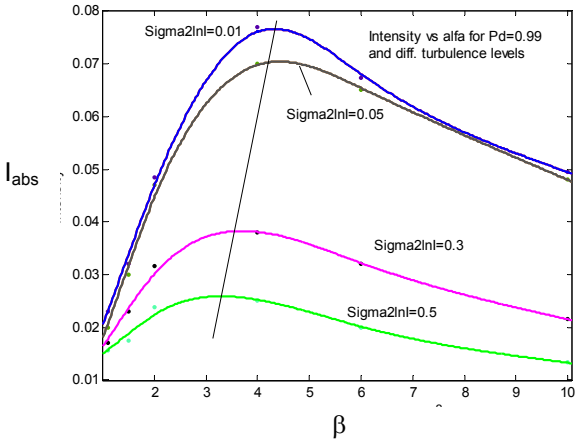

Figure 9. Absolute intensity (scaled with α) vs β and Pd($I>I_{min}$) = 0.99. Different turbulence levels are indicated by σ^2_{lnI}.

The tracking error can be calculated as a function of the beam parameter for different perturbation magnitudes. In
Figure 10 some results showing of tracking accuracy obtained at different turbulence strength are presented. See, Appendix – Tracking optimisation using signal statistics for a definition of the normalised tracking error.

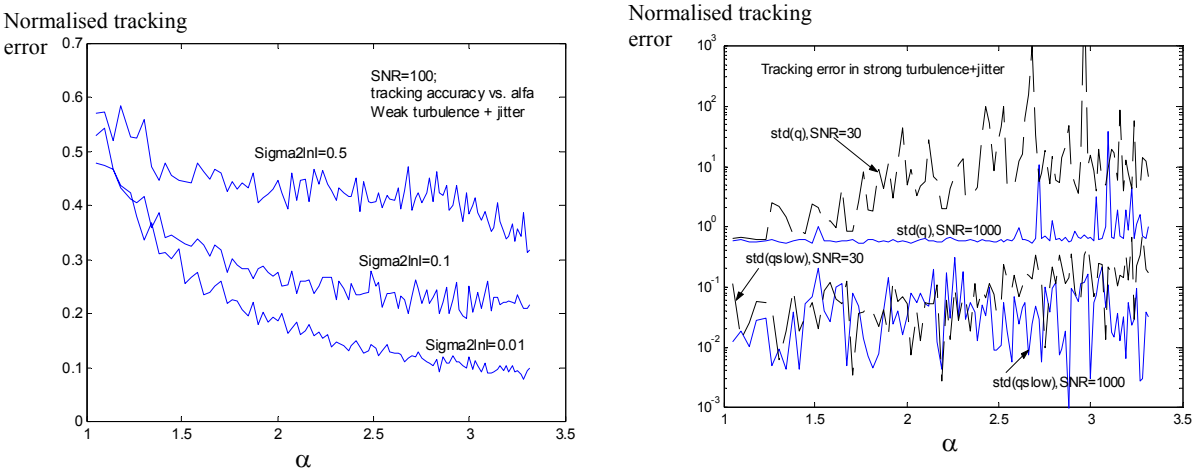

Figure 10 Normalised tracking error vs. α. Weak turbulence and jitter (left) and strong turbulence and jitter (right - different nominal SNR, without jitter, are given in the figure).

The normalised tracking error decreases monotonously as a function of α in weak atmospheric turbulence as indicated in Figure 10. Depending on the turbulence strength an optimal α can be found where the

normalised tracking error becomes constant. At higher turbulence levels this value this value decreases as anticipated. In presence of strong turbulence and jitter the normalised tracking error increases considerably. A summary of the results from the calculations is given in the appendix.

4. AERO-OPTICAL EFFECTS

A comprehensive monograph describing various aero-optical phenomena, measurement methods, experimental results and system performance degradation can be found in ref. [16]. Aero-optical phenomena differ from atmospheric perturbations in such way that they originate from the moving flow-fields about an aircraft (Figure 11). Variations in the air density close to the fuselage of the aircraft can be associated to changes in the refractive index. These effects cause beam wander and beam broadening which reduce the instantaneous and averaged beam intensity on the target. Apart from aero-optical effects originating from the airflow acoustic effects induced by aero-optical phenomena may be large. However, in this paragraph only effects due to the aero-optical flow field are considered and it is assumed that the induced acoustic effects have been minimized.

Effects defining aero-optical phenomena include:

- Density fluctuations in the flow-field which cause index of refraction variations i.e. boundary and shear layer turbulence
- Inviscid flow-field appearing in the vicinity of turrets and apertures
- Shock effects induced at super sonic velocities

In the treatment below phenomena due to turbulence in the boundary layer, shock and inviscid flow are considered quantitatively. Aero-optical effects occurring at velocities below 0.3 Mach are considered to be negligible [17].

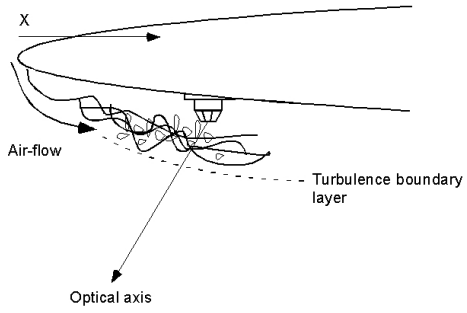

Figure 11 Aero-optical effects appearing close to the aircraft fuselage.

An excellent review covering recent advances in the field of aero-optical phenomena has been presented by Jumper and Fitzgerald[18]. Their article includes an extensive reference list dedicated to AO phenomena.

4.1 Theoretical models

Accurate theoretical models based on analytical expressions describing aero-optical effects in combination with laser beam propagation are not available. In this section some expression relevant for estimating magnitudes of aero-optical phenomena are presented. Since AO-effects originate from complicated

physical phenomena involving turbulence and shocks the results presented in the paragraph below are to be considered as “rule of thumb” estimates. For more advanced treatment full CFD calculations based on solving Navier-Stokes equations with proper boundary conditions are required to calculate optical properties and effects due to the flow field.

4.1.1. Strehl ratio

One figure of merit commonly used to express laser beam degradation is the Strehl ratio [19]. The Strehl ratio is defined as the ratio between the on-axis intensity of a perturbed laser beam divided by the on-axis intensity of the diffraction-limited counterpart i.e.

$$S = \frac{I^o_{aberr}(t)}{I^o_{diff}}.$$

In general, the Strehl ratio is time dependent but often the averaged Strehl is considered for judging the influence of perturbations. The Strehl ratio can also be expressed in terms of the wave front phase variance according to

$$S \approx e^{-\sigma_\Phi^2} \qquad \text{eq. 20}$$

where σ_Φ^2 is the wave front variance. The wave front distortion can also be expressed in terms of the wave aberrations, σ_w

$$\sigma_\Phi = \left(\frac{2\pi}{\lambda}\right)\sigma_w. \qquad \text{eq. 21}$$

Thus, laser beam degradation due to phase-induced aberrations are expressed as a loss in Strehl ratio. Using the definition above a diffraction limited beam has $S = 1$. If the contributions to the wave front aberration are statistically independent the different contributions can be added according to

$$S = e^{-\left(\sum_{i=1}^{N}\sigma_i^2\right)}. \qquad \text{eq. 22}$$

The Strehl ratio is used throughout this paragraph as a figure of merit to account for a reduction in brightness in front of the seeker aperture due to laser beam degradation effects having their origin from aero-optics. It is interesting to illustrate how the Strehl ratio depends on the wavelength (Figure 12). At shorter wavelengths the Strehl decreases dramatically for a given flow field. Below $\lambda = 1.0$ μm the effect causes a severe reduction in Strehl which reduces the overall irradiance. The illustrative example was assuming a flow field giving a Strehl, $S = 0.95$, at $\lambda = 10$ μm. The variation of the on-axis irradiance for a diffraction-limited laser beam, on the other hand, decreases as a function of wavelength due to diffraction effects. This behaviour is depicted in Figure 12 where the irradiance is plotted as a function of wavelength for a given transmitter configuration.

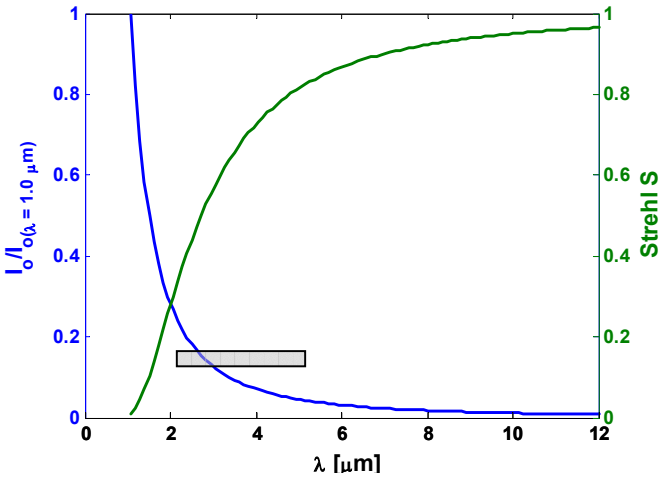

Figure 12 Normalised on-axis irradiance as a function of wavelength. The irradiance was normalised to the value observed at λ = 1.06 μm (solid-blue). Strehl ratio plotted as a function of the wavelength. A Strehl ratio of 95% was assumed at λ = 10 μm. The grey bar represents the wavelengths used by DIRCM systems.

Considering a DIRCM transmitter operating in the 2 to 5 μm wavelength region the Strehl ratio may vary considerably due to aero-optical effects. This fact necessitates a detailed analysis of the magnitude and sources of the AO-effects contribution to the overall performance degradation of a DIRCM system.

4.1.2. Boundary- and shear layer turbulence

The wave front distortion due to rapidly moving flow fields creating shear and turbulence layers close to the aircraft fuselage can be estimated from the Gladstone-Dale relationship

$$\sigma^2 = 2G^2 \int_0^L \langle \rho^2 \rangle l_z dz, \quad l_z << L \qquad \text{eq. 23}$$

where σ^2 is the wave front variance, l_z the correlation distance for the perturbation, ρ the air density and G the Gladstone-Dale constant. The bracket defines the averaged density fluctuations along the path. The Gladstone-Dale equation relates the changes in the air density to a change in the refractive index according to

$$n = 1 + G\rho\,. \qquad \text{eq. 24}$$

The Gladstone-Dale coefficient is almost constant in the mid-infrared wavelength region (Figure 13), which means that the index of refraction is mainly dependent on the alteration of the air density due to the flowing field about the platform.

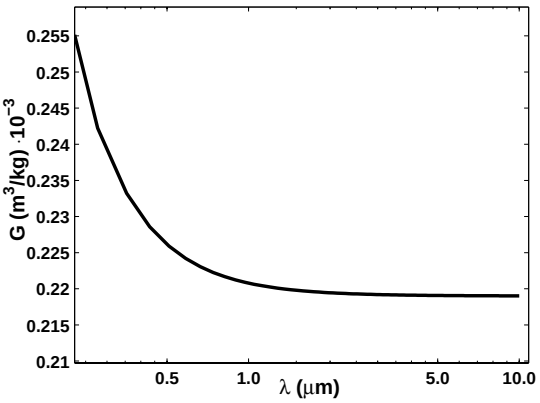

Figure 13 Variation of the Gladstone-Dale coefficient as a function of wavelength.

The most characteristic properties of boundary- and turbulent shear layers are summarized in Table 1. Aero-optical effects can now be estimated by utilising the Gladstone-Dale relationship to calculate the influence from the boundary (and shear) layer. The width of the boundary layer depends on the distance to the leading edge. This fact makes a pod installation favourable, and particularly, if the aperture can be located close to the leading edge of the pod. The turbulent shear layer has it origin from obstacles and discontinuities on the aerodynamic surface. The boundary layer, on the other hand, is defined from the leading edge. The scale of the shear layer is slightly larger than the corresponding boundary layer (Table 1). Since the shear in the flow field is dependent on the local geometric arrangement accurate calculations are required to treat these effects in detail.

Table 1 Properties of AO boundary- and shear layers[1]

Parameter	Boundary layer	Shear layer	Comments
Extent of layer	$L \propto X^{0.8}$	$L \propto 0.25X$	L_{BL} ~ 10-50 cm (experimental data)
Correlation scale	$l_z = 0.10$L	$l_z = 0.20$L	l_z ~ 1-3 cm
Density variation	$\rho' \sim 0.1(\rho_o - \rho_w)$	$\rho' \sim 0.1(\rho_o - \rho_c)$	ρ_c = cavity density ρ_o = free-stream density ρ_w = wall density

[1)] X = distance from the leading edge, l_z = correlation distance, L = width of turbulence/shear layer.

The scattering angle due to turbulence- and shear layers can roughly be estimated according to

$$\theta = \frac{\lambda}{l_z}. \qquad \text{eq. 25}$$

where l_z is the correlation distance of the turbulence cells within the layer. The extent of the turbulent (boundary) layer, L, can be calculated using the following relation (valid for a flat plate),

$$L = 0.37X\left(\frac{uX}{\nu}\right)^{-\frac{1}{5}} \qquad \text{eq. 26}$$

where X is the distance from the leading edge causing the boundary layer, u is the free-stream velocity and ν the kinematic viscosity of the flowing air. The kinematic viscosity of air vary from $\nu = 1.46 \cdot 10^{-5}$ m^2/s at sea level to approximately $\nu = 2.21 \cdot 10^{-5}$ m^2/s at 5000 m altitude. Using eq. 26 to calculate the extent of the turbulent boundary layer the thickness vary from L ≈ 8 to 14 cm from the midpoint of the fuselage to the end (X = 7.5 to 15 m, Figure 14A). The width of the TBL decreases at higher altitude if a higher platform velocity is assumed.

The density variations $\langle \rho^2 \rangle$ utilised in eq. 23 can be calculated with knowledge about the density variation in the boundary layer. An example showing how the density varies from the wall of the platform to the free-stream value as a function of the Mach number is depicted in Figure 14B. Increasing the flow velocity from 0.3 to 2.0 Mach the wall density reduces approximately 40 % in comparison to the free-stream air density, ρ_o.

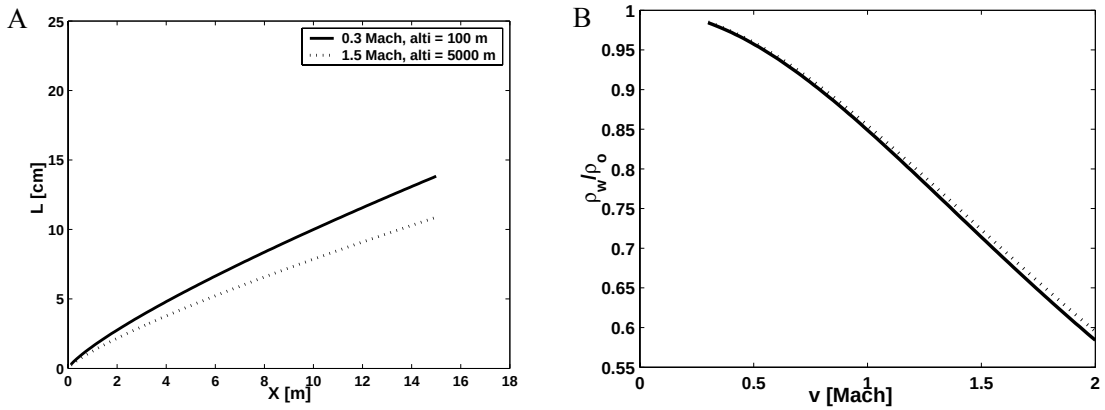

Figure 14 a) TBL extent (L) as a function of distance from the leading edge (X) for two different situations. b) Variation of the air density close to the aircraft wall as a function of the velocity of the air stream (solid line–turbulent flow, dotted line-laminar flow).

The boundary layer also exhibits laminar flow where the difference in density close to the fuselage causes a variation in the index of refraction. This effect is more or less quasi-static from optical point of view and gives rise to a lens and refractive phenomena. At Mach 2 and sea level conditions is the lens effect very weak (F ~ 10^8 m, 30 cm from leading edge) and can be neglected. The other effect associated with laminar flow in the boundary layer is a deflection of the optical axis due to the variation of the refractive index. This wedge effect is of the order of ~1 μrad under the same conditions as above and can consequently be neglected. It should also be noted that this effect is self-corrected in a mono-static system.

4.1.3. Inviscid flow effects

The inviscid flow effects need to be considered because of compressible airflow close to the DIRCM turret. Generally, low order aberrations such as tilt, focus/defocus and astigmatism are associated with inviscid flow. These effects can rather easily be corrected by using adaptive optics for aberration compensation.

Otten and Gilbert have investigated inviscid flow-field effects on laser turrets in wind tunnel experiments[20]. Experimental data form the wind tunnel experiments were correlated with an empirical model describing the AO-effects from the inviscid flow field. It was concluded that the effects due to compressible flow around the turret are of second-order, in comparison to TBL and TSL effects, at longer wavelengths. A weak focusing effect was observed and a phase shift of $\sim 7 \cdot 10^{-4}$ cm was registered across the aperture. It should be noted that the results presented by Otten and Gilbert concerned a rather large turret and optical aperture. In a DIRCM installation on a FJ is the turret much smaller and the aperture dimensions of the order; 2-4 cm diameter for the laser beam and ~ 10 cm diameter for an imaging channel. Thus, due to the smaller aperture dimensions the effect on the DIRCM transmitter are probably larger than those reported by ref.[20].

The phase distortion introduced by a hemispherical turret has been estimated using a model developed by Fuchs and Fuchs [21]. An analytical expression was derived for a turret situated on the fuselage and with a circular beam cross section. The expression for the phase distortion due to inviscid flow can be estimated according to the following integrals [21]

$$\Phi = \frac{\kappa'}{\lambda}\frac{\rho_\infty}{\rho_{SL}} R \int_0^s \frac{\rho - \rho_o}{\rho_\infty}\frac{ds}{R} + \frac{\kappa'}{\lambda}\frac{\rho_\infty}{\rho_{SL}} R \int_{-s}^0 \frac{\rho - \rho_r}{\rho_\infty}\frac{ds}{R}. \qquad \text{eq. 27}$$

The following definitions were used: ρ_∞ , ρ , ρ_o is the free stream air density, the local gas density and the density at the sea level, respectively. κ' is a constant and R is the diameter of the outgoing beam. An example from their model is depicted in Figure 15 where the phase distortion across the aperture is shown for two different directions of the beam and a free stream velocity corresponding to 0.59 Mach. The turret and beam dimensions used in their calculations were much larger than the size anticipated for a DIRCM system situated on a FJ platform. As pointed out above the two major contributions to inviscid flows is focusing/defocusing and tilt errors. This statement is supported by the model calculations showing a focusing effect (Figure 15A) when the beam is directed parallel to the airflow and a tilt distortion when the beam is directed in a non-parallel direction (Figure 15B).

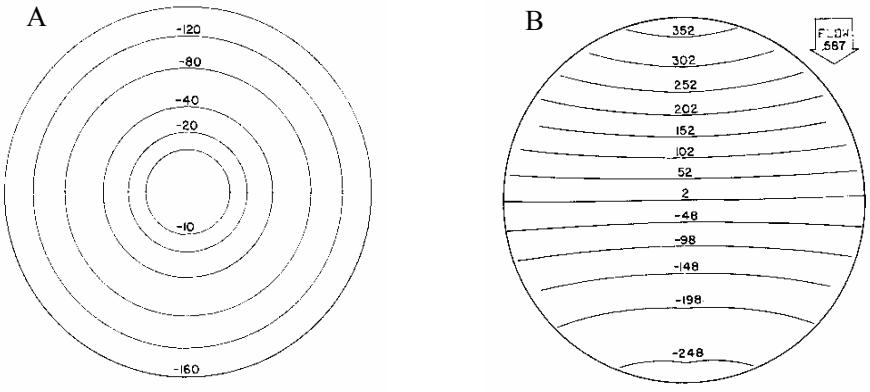

Figure 15 Estimated phase distortions due to inviscid flow effects about a hemispherical turret. A) Beam is pointing in the fore direction. B) The angle between the air stream and the outgoing beam was 54°**.** The numbers are in units of 100·waves. The wavelength was λ = 3.8 μm. From ref. [21].

The following scaling relation can be used to estimate the phase distortion under different conditions

$$\frac{\Phi_2}{\Phi_1} = \frac{\lambda_1}{\lambda_2}\frac{\rho_2}{\rho_1}\frac{R_2}{R_1}\frac{\kappa_2'}{\kappa_1'} \qquad \text{eq. 28}$$

where λ_i is the wavelength, ρ_i is the air density, R_i is the turret radius and κ_i is a constant. From eq. 28 estimates at different conditions can be made. For example, since the air density decreases exponentially with altitude the aberration due to inviscid flow field are less pronounced at higher altitudes.

4.1.4. Chock effects

Aero-optical shock effects occur during the transition from the trans-sonic to super-sonic velocities. The formation of a shock wave depends on several parameters such as the local turret geometry, altitude and the local Mach number. The critical Mach number $M \cong 0.57$ indicates the first appearance of a shock wave. Depending on the local geometry the shock wave can be situated close to the turret (leading edge) or as for larger body a distance ahead. Conical and wedge flow are the most common situations for establishing shock waves. The shock waves can be considered as quasi-stationary and acts as a refractive surface for the outgoing laser beam or incoming optical field. Optical effects associated with aero-optical shock waves include refraction effects, focal length variations and reflection at the shock wave boundary.

The refractive effect at the shock wave boundary causes a deflection of the laser beam, which can be calculated using Snell's law and the variation in air density in front of and behind the shock boundary. In Figure 16A an estimate of the tracking error is depicted for an optical axis approaching the shock wave front at an angle of incidence, $\beta_o = 35^o$. This case represents a situation close to the worst case with respect to the optical axis orientation relative the shock wave front. The tracking error decreases as the optical axis approaches the perpendicular direction relative the shock plane. It should be pointed out that a mono-static system does not suffer significantly from refractive shock effects since the tracking error is compensated by a deflection of the beam. Refractive effects can probably be neglected in a DIRCM-system since a common optical aperture is employed for transmit and receive channels.

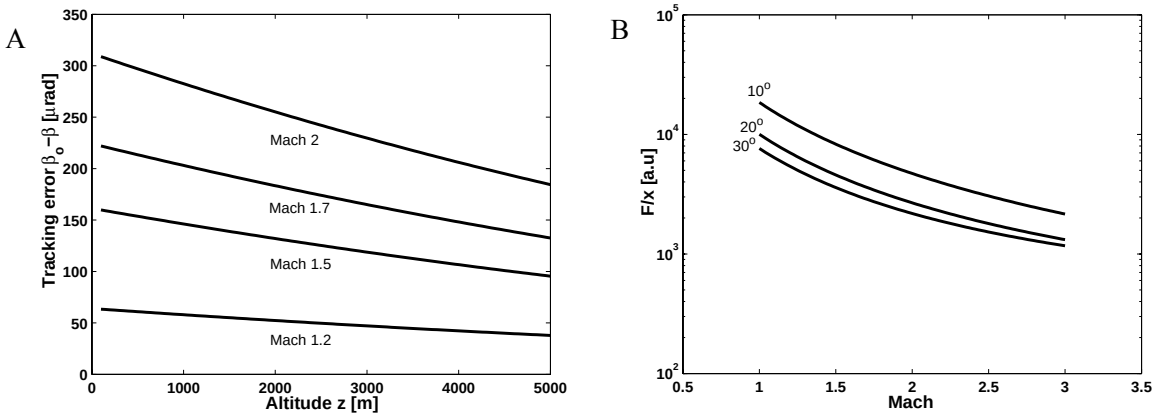

Figure 16 A) Tracking error as a function of altitude and Mach number for refractive shock effects. B) Ratio between the focal length and distance to conical apex as a function of Mach number for different deflection angles.

If the discontinuity creating the shock wave has a curved surface the shock wave itself appears as curved. In this case is the deflection angle dependent on where on the shock boundary the ray intercepts. For example, in the case of a conical shock wave the imposed wave front aberration resembles a lens that has a focusing effect on the beam (Figure 16B). The shock wave formed in front of a hemispherical turret produces an effective focal length, which varies depending where on the shock wave the ray hit. The effective focal length is approximately 3 orders in magnitude larger than the radius of the hemispherical transmitter in this example. For a typical DIRCM transmitter having a turret radius with ~25 cm diameter and an outgoing beam with 1-3 cm diameter the negative lens effect from the shock wave is estimated to

be F ~ 250 m ($F \approx 10^3 \cdot D_{hemisphere}$). Interpreting this negative lens effect in terms of wave front aberration for the outgoing laser beam a wave front error of the order $\sigma \approx \frac{\lambda}{100} \sim \frac{\lambda}{70}$ which corresponds to a Strehl ratio, S ~ 0.99. The reflection of the optical field at the shock wave boundary is small (less than 10^{-6}) and can be neglected regarding the power in the outgoing laser beam. Reflected power due to the shock boundary contributes to an increased optical noise in the receiver channel.

In summary the effects from inviscid flow and shock can be neglected or corrected for by introducing adaptive optics. Both these effects introduce low order aberrations with slow temporal variations. By carefully designing the geometry of the DIRCM transmitter the influence from these effects can be minimized.

4.1.5. Sample calculations

In order to estimate the influence of AO-effects on a DIRCM system for fast jet application sample calculations regarding effects from TBL and TSL have been carried out. Three different cases have been considered whereas case I defines a low altitude scenario corresponding to surface-to-air missile threat during landing- or take-off. Scenario II and III define high altitude examples where the aircraft may be engaged in a dogfight (scenario II/III) or the threat is fired from the ground (scenario II). Different parameters such as e.g. influence of the altitude, Mach number and the location of the DIRCM system on the platform have been analysed.

Table 2 Parameters used to in sample calculations

Scenario	**ρ_o [kg/m^3]**	**<ρ> [kg/m^3]**	***l_z*** [m]	***L [m]***	***X [m]***	***G [m3/kg]***	***h***
I	1.210	0.0066	0.1·*L*	0.08	7.5	$0.22 \cdot 10^{-3}$	100
II	1.106	0.0066	0.1·*L*	0.06	7.5	$0.22 \cdot 10^{-3}$	1000
III	0.722	0.028	0.1·*L*	0.07	7.5	$0.22 \cdot 10^{-3}$	5000

The effect of a turbulent boundary layer can be estimated using formulas presented in ref. [22]. If we employ the parameters depicted in Table 2 the following estimates of the wave front degradation due to boundary layer turbulence are obtained (TBL-effects are considered to be the most critical perturbation source of the wave front). It was assumed that the transmitter was located at midpoint i.e. *X* = 7.5 m from the platform leading edge. A pod installation reduces the effects from TBL considerably since X is reduced.

Scenario I

This scenario is a low-altitude sub-sonic situation occurring close to landing or take-off. A typical threat is shoulder-launched IR-guided missile. In the scenario the platform velocity is assumed to be low i.e. 0.3 Mach. The main parameters for this situation are defined in Table 2 and we assume that the wall air density is 6 % lesser than the free-stream atmospheric value i.e. $\rho_{wall} \approx 0.94\rho_o$ (see Figure 14) which corresponds to Mach 0.3. The average variation of the air density in the boundary layer can be approximated as $\langle \rho \rangle \approx (\rho_o - \rho_{wall}) \cdot 0.1$. The TBL thickness (calculated using eq. 26) is *L* = 8 cm at the mid-point of the fuselage. This value is slightly lower than those reported experimentally [16,17]. According to eq. 23 above the following wave front error is obtained: $\sigma \approx G\langle \rho \rangle (2 l_z L)^{\frac{1}{2}} \approx 0.01$ waves at λ = 4 μm. This wave front error corresponds to the case where the laser beam is directed perpendicular to the flow

direction ($\theta = 90^o$). The wave front degradation and the corresponding Strehl ratio increase when the angle between the flow direction and the beam decreases, as shown in Figure 17. The worst condition is obtained when the beam is parallel to the flow that corresponds to the case when the beam is pointing in the aft direction.

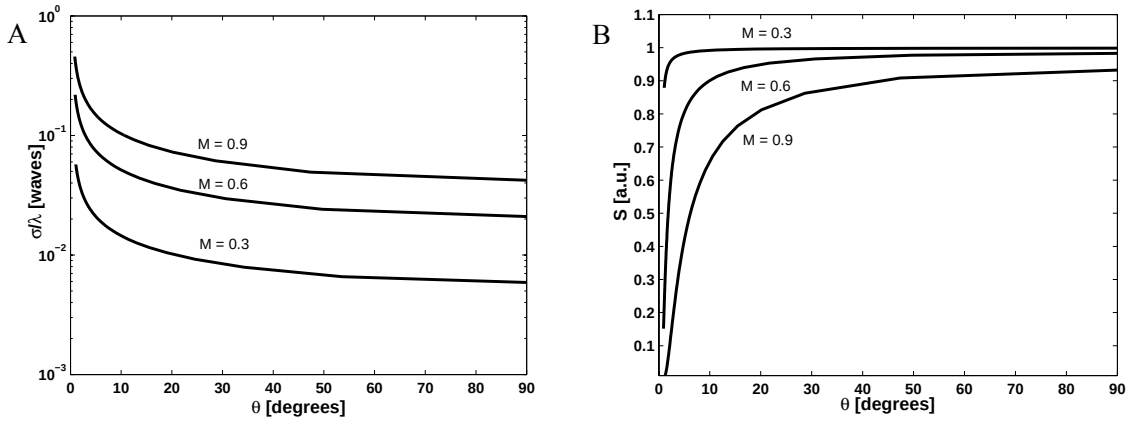

Figure 17 A) TBL wave front aberrations as a function of relative pointing angle ($\theta = 90^o$ correspond to a beam pointing parallel to the TBL layer). B) Strehl ratio (I/I_o) as a function of pointing direction. The different curves correspond to different Mach numbers.

At low Mach numbers is the influence from the TBL effects small as depicted in Figure 17. The Strehl ratio is $S > 0.8$ for pointing angles $\theta > 20^o$ and in the perpendicular direction is the Strehl $S > 0.9$. The dramatic reduction in the Strehl ratio only occurs when the beam is directed parallel and within the TBL layer.

Scenario II

The second scenario is at higher altitude, z = 1 km and describes a supersonic situation whereas the Mach number vary between 1.0 to 2.0 Mach. The wall density is approximately $\rho_{wall} \approx 0.85\rho_o$ due to the increased Mach number and the wave front error $\sigma \approx G\langle\rho\rangle(2l_z L)^{\frac{1}{2}} \approx 0.05$ waves at λ = 4 μm which corresponds to $S \approx 0.91$. The variation of the Strehl ratio as a function of beam direction is shown in Figure 18. The Strehl ratio decreases as the platform velocity increases and at 2.0 Mach is the peak on-axis intensity reduced approximately 50% for a beam pointing perpendicular to the flow direction. At lower mach numbers, M ~ 1.0, vary the Strehl between 0.8-0.9 for beam directions, $\theta \sim 30 - 90^o$. The most dramatic alteration of the Strehl ratio occurs in beam directions nearly parallel to the flow direction as above.

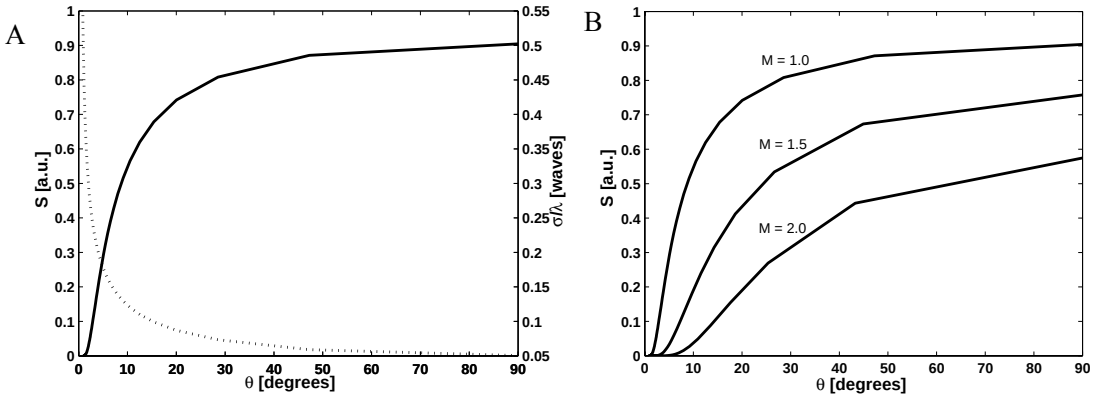

Figure 18 A) Variation of the Strehl (solid)/wave front error (dotted) as function of pointing direction for scenario II. The Mach number was 1.0 and 1 km altitude. B) Strehl as a function of beam direction at different Mach numbers.

Scenario III

This scenario is similar to II with the exception that the altitude is increased to z = 5 km. A supersonic situation i.e. 1.0-2.0 Mach is considered also in this case. At 5 km is the air density reduced 28% in comparison to the sea level The wall density is approximately $\rho_{wall} \approx 0.85\rho_o$ due to the increased Mach number and the wave front error $\sigma \approx G\langle\rho\rangle(2l_z L)^{\frac{1}{2}} \approx 0.03$ waves at $\lambda = 4$ μm which corresponds to $S \approx 0.96$ ($\theta = 90^o$, $M = 1.0$). The Strehl ratio plotted as function of the beam direction is depicted in Figure 19 for different Mach numbers. No major difference in the Strehl ratio is obtained in this case in comparison to scenario II.

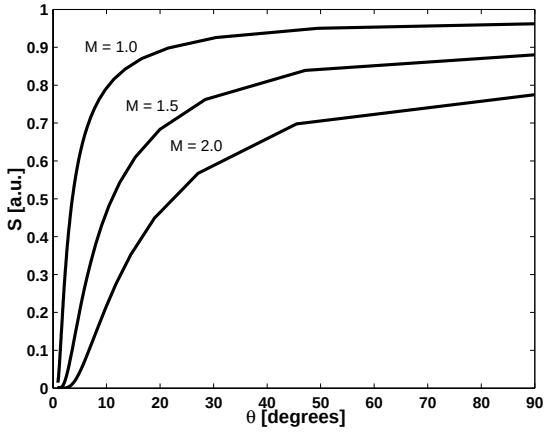

Figure 19 Strehl ratio as function of beam direction for different platform velocities (scenario III). The altitude was z = 5 km.

The wavelength and the location of the transmitter are two parameters that heavily influence the effects on beam quality from turbulence in the boundary layer. In order to illustrate the wavelength dependency the Strehl ratio is plotted as a function of the wavelength in Figure 20A. At shorter wavelengths the Strehl ratio drops significantly due to the increase of the Gladstone-Dale parameter. For example, a decrease in Strehl from S ≈ 0.97 to 0.83 at λ = 4.0 to 1.5 μm can be observed at Mach 1.0. Increasing the platform velocity to Mach 2 implies further decrease in the Strehl ratio and S < 0.35 is obtained at λ ~ 1.5 μm.

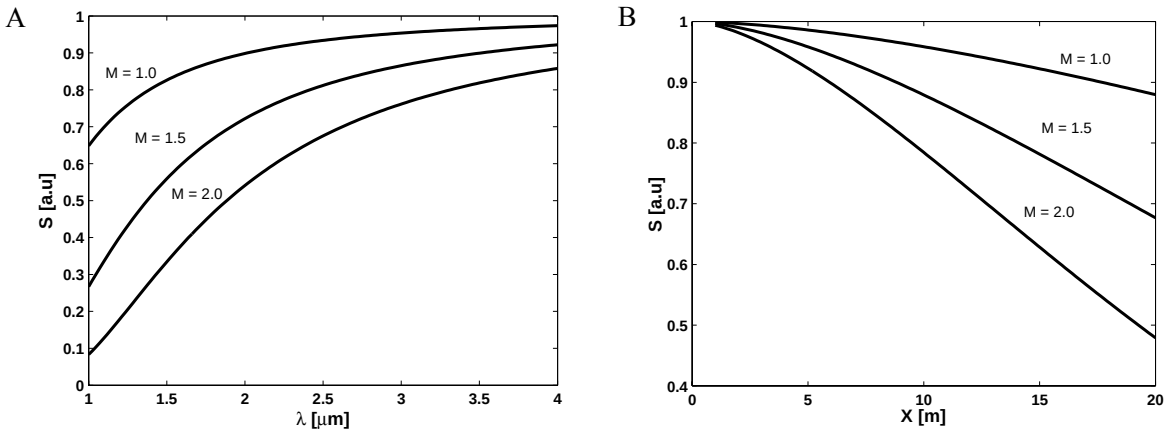

Figure 20 A) Strehl ratio as a function of wavelength for scenario II, Mach 1.0, $\theta = 90^o$. B) Strehl ratio as a function distance to the leading edge (scenario II, Mach 1, $\theta = 90^o$).

As mentioned above the wave front degradation also critically depends on the location of the DIRCM transmitter relative the leading edge. This is due to the fact that the thickness of the TBL layer increases moving the transmitter further away from the leading edge. The reduction in Strehl increases at higher velocities as depicted in Figure 20B.

It should be noted that the sample calculations presented above represents worst cases of TBL effects since the height of the DIRCM transmitter turret reduces the propagation length in the turbulent boundary layer close to the fuselage. A careful design and optimisation of the geometry of the turret reduces the effects form the TBL considerably. Another issue important to address is the temporal evolution of the TBL effects. Experimental results from wind tunnel experiments and flight tests have shown time scales of the order of 1 to 5 kHz or higher. This fact makes optical corrections of TBL layer effects a very delicate task. Although the examples above did not include specific conditions they provide information about the order of magnitude of wave front error, which can be expected from aero-optical phenomena.

4.2 Experimental data

The purpose of this paragraph is to briefly summarise some experimental data on aero-optical effects presented in the literature. However, it should be kept in mind that the actual location of the DIRCM system on the aircraft, type of aircraft, flight conditions and the geometrical design of the APT head are some parameters that heavily influence the aero-optical effects. This paragraph only contain references to field experiments carried out under real flight conditions i.e. wind tunnel results and similar activities are excluded. The idea is to investigate whether results can be extrapolated to the scenario descriptions in order to estimate order of magnitudes of the different aero-optical phenomena.

Several test studying aero-optical phenomena during real flight conditions were performed in USA during the period 1970-80. Extensive programs such as the *LEAR Jet* and *ALL Cycle* provided new knowledge on AO near-field phenomena. One major effort during this period was to verify wind tunnel results during flight conditions and derive the necessary scaling laws tying AO and aerodynamics together. A comprehensive summary of the results obtained in these experiments can be found in ref. [23]. Early discovered in these experiments was the fact showing the insensitivity of longer wavelength towards AO-effects. Wide-ranging flight tests were performed in these programs studying AO-effects at altitudes ranging from 0.2 to 15 km and at subsonic Mach values (0.2-0.9). Some experimental results from the trials described above are presented in Table 3.

Experimental results studying the turbulent boundary and shear layers about a KC-135 aircraft fuselage have been presented by Craig and Allen [24]. The experimental results from flights with varying altitude (1.8-10.7 km) and at different Mach numbers (M = 0.3-0.7) were presented. Phase deviations observed for the boundary layer were of the order of $\sigma = 0.06$ to 0.17 waves at $\lambda = 0.53$ μm with piston and tilt terms removed. For artificially generated shear flow the wave front degradation was of the order of $\sigma = 0.10$ to 0.28 waves at $\lambda = 0.53$ μm with piston and tilt terms removed. It was also reported that the low order aberrations had a lower characteristic frequency (1-5 kHz) in comparison to high order aberrations (10-20 kHz).

Table 3 Literature results on experimental data reported on aero-optical effects

Platform	Mach	Altitude	l_z	Perturbations	Comments	Ref.
KC-135 aircraft	0.3-0.8	1.8-10.7 km	2 cm	BL σ_{BL}~ 0.06-0.17 waves @ $\lambda = 0.53$ μm SL σ_{SL}~ 0.10-0.28 waves @ $\lambda = 0.53$ μm (piston/tilt contribution removed)	Temporal response 1-5 kHz	[24]
LEAR jet	0.3-0.8	1.5-12 km		BL σ_{BL}~ 0.08-0.11 waves @ $\lambda = 0.63$ μm SL σ_{SL}~ 0.10-0.16 waves @ $\lambda = 0.63$ μm (tilt contribution removed)		[25]
KC-135 aircraft	0.2-0.8	0.3-11 km	1-3.5 cm	BL σ_{BL}~ 0.08-0.18 waves @ $\lambda = 0.63$ μm SL σ_{SL}~ 0.08-0.26 waves @ $\lambda = 0.63$ μm (tilt contribution removed)		[26]

The wave front degradations reviewed in Table 3 can be scaled in wavelength. Assuming that the characteristic correlation length, l_z, of the turbulence is smaller than the aperture i.e. $l_z < D$, the following simple scaling relation can be used

$$S = \frac{I}{I_o} e^{-\left(\frac{2\pi\sigma}{\lambda}\right)^2} . \qquad \text{eq. 29}$$

Scaling the values obtained in the visible wavelength region to the value decided to, $\lambda = 4.0$ μm, result in a considerable increase in the Strehl ratio (Table 5). For example, the values obtained in the Lear jet test, $\sigma_{BL} = 0.08$ - 0.11, for the boundary layer turbulence corresponding to a Strehl, S = 0.78 - 0.62, increases to $S \approx 0.99$ at $\lambda = 4.0$ μm.

Thus, the conclusion obtained scaling experimental data to the mid-ir wavelength region is that the influence from boundary- and shear layer turbulence close the aircraft fuselage is considerably reduced. This conclusion also agrees with the calculated results presented above in this report.

4.3 Computational fluid dynamics calculations

During recent years computational fluid dynamic (CFD) calculations have been employed to calculate aero-optical effects occurring in aerodynamic flow-fields around aircrafts. Using the Gladstone-Dale relationship parameters obtained from CFD codes can be translated into phase aberrations introduced by the flow-field. Pade recently showed how existing CFD codes could be utilised to calculate AO-effects occurring at super- and hypersonic velocities (up to Mach 9) [27]. Another example involving CFD calculations of optical turbulence through aero dynamical flow fields and wakes was presented by Jones and Bender [28]. An analysis of aero-optical effects stemming from an aircraft fuselage and optical turret configuration was presented. The analysis contained temporal aspects of the wave front errors, far-field laser beam profile and low order correction modes etc. Interestingly, the temporal behaviour for the different low-order perturbations (tilt in x/y) can be calculated which provides information about e.g. requirement for a fast steering mirror in a high precision APT unit.

5. PLUME AND WAKE EFFECTS

5.1 Turbulence effects in jet engine plumes

Effects of laser beam propagation through a jet engine plume have been investigated with the aircraft tethered to the ground [29]. The ground imposes constraints in this configuration but the effects originating from the boundary were neglected in the investigation. The purpose with the experimental study was to determine the strength of the turbulence, i.e. the structure parameter C_n^2, and estimate the motion of the beam centroid (beam wander) due to effects from the engine plume. Direct imaging using a camera was used to monitor the beam profile degradation. The laser acts like a point source and the degradation and the motion of the beam centroid due to the plume can be registered. The value of C_n^2 can be determined from the *MTF* by adopting an appropriate model taking care of the variation of C_n^2 along the path and fitting the theoretical model to experimental results. From the total integrated C_n^2 the contribution from the plume can be deduced. The motion of the beam centroid can be calculated directly from the information provided by the captured the images.

5.1.1. Experimental procedure

The aircraft was secured and located on the ground. The exhaust plume exited the aircraft horizontally approximately 3 m above the ground. A HeNe laser (λ = 633 nm) was used as light source and the laser beam intersected the jet plume diagonally. A CCD camera was used to capture instantaneous images of the beam profile after passage through the plume. The camera operated at 25 Hz frame rate and the exposure time was 100 μs. The distance between the laser and the camera was 220 m and the part of the path crossing the plume was approximately 20 m. The experimental set-up is depicted in Figure 21.

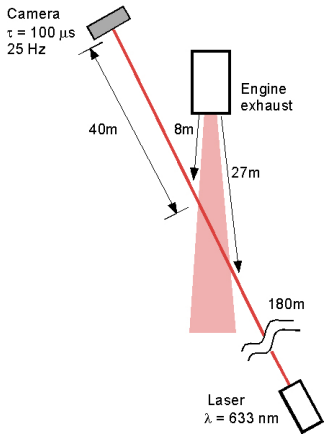

Figure 21 Experimental set-up for studying jet engine plume effects on laser beam propagation.

Three different engine throttle levels (labeled I-III), using the afterburner, were employed. The geometric extent of the plume was estimated to a 20-degree divergence cone in the turbulent mixing zone. Before each registration of the beam profile with the camera a reference image was recorded at different throttle strengths. The *MTF* and beam wander were calculated from separate recordings. Integrated structure parameters (for the path intersecting the plume) and root-mean-square (rms) values for the motion of the beam centroid were determined for the different throttle strengths. The C_n^2 was calculated from the experimental data using a model based on a $R^{-2/3}$ decay (R defines the distance from the engine exhaust) of the structure parameter within the plume.

5.1.2. Experimental results

The measured quantities included the angular spread (beam broadening), centroid motion (beam wander) and the magnitude of the structure parameter in the plume. The observed structure parameter, $C_n^2 = 3 \cdot 10^{-9}$-$1.5\ 10^{-8}$ $m^{-2/3}$, is 3 to 4 orders of magnitude higher than the value commonly observed close to ground in normal conditions ($C_n^2 \sim 10^{-14}$ $m^{-2/3}$). The structure parameter depends on the throttle strength, as depicted in Table 4, and increased approximately 5 times between the lowest and highest utilized strength. The beam divergence increased from 0.7 to 8.7 mrad during propagation through the plume. The major contribution to the beam broadening is due to the turbulence effects caused by the moving gases within the plume. Motion of the beam centroid was observed during propagation through the plume. The rms value increased from 0.8 to 2.5 mrad for throttle strengths I-III, respectively.

Table 4 Summarized results – laser beam propagation through a jet engine plume [29]

Case	Beam wander σ_{rms} [mrad]	Angular spread [mrad]	Structure parameter C_n^2 [$m^{-2/3}$]
Ref.		0.7	
I	0.8	3.2	$3x10^{-9}$
II	1.3	4.4	$4x10^{-9}$
III	2.5	8.7	$1.5x10^{-8}$

The experimental parameters determined can be compared with expected values from propagation of a similar distance using a horizontal path close to ground. Here, we assume Rytov theory to be valid due to the short propagation constant and the turbulence strength is $C_n^2 = 10^{-13}$ $m^{-2/3}$ which corresponds to an averaged Diurnal value close to ground. The rms beam wander can be estimated from the image dancing of the beam centroid. Another condition, which needs to be fulfilled, is that the inner scale, l_o, should be less than the aperture i.e. $l_o << D$. The magnitude of beam wander in this case is several orders of magnitude smaller than the observation made for propagation through the jet plume and scales linearly with C_n^2.

5.1.3. Results reported in literature

Early studies of laser beam propagation through a jet engine (J-57) exhaust were carried out by Hogge and Kasinski [30]. They used a HeNe laser (λ = 633 nm) to study beam broadening during laser beam propagation through the exhaust at different locations and calculated the structure parameter, $C_n^2 \sim 10^{-10}$-10^{-11} $m^{-2/3}$. Barrett and Budni have also studied laser beam propagation through a jet plume [31]. They reported a structure parameter, $C_n^2 = 3 \cdot 10^{-9}$ $m^{-2/3}$, a wandering of the beam centroid 100 - 200 μrad and an increase of the beam radius with a factor two. The variation of C_n^2 along the plume was modelled using an exponential decay function

$$C_n^2(R) = C_n^2(0) \cdot e^{-\frac{R}{\kappa}} \qquad \text{eq. 30}$$

where $C_n^2(0)$ is the structure parameter close to the engine exhaust and κ is a decay constant. An approximate expression for calculating the amount of beam broadening in presence of strong turbulence was presented. The exponential decay constant, κ = 0.045 m^{-1}, was determined from the experimental data.

Table 5 Experimental results – effects on laser beam propagation in jet engine plumes

C_n^2 [$m^{-2/3}$]	Beam wander σ [mrad]	Scintillation index - β2	Brodening <Δw0>	Comments	Ref.
$4 \cdot 10^{-10}$	0.052 (λ = 1.06 μm) 0.054 (λ = 10.6 μm)	0.5±1 (1.06 μm, far-field)		λ = 0.53,1.06,10.6 μm, L = 26 cm, l_0 = 1.7 mm	[32]
(2-5) 10^{-10}	~ 0.10 (λ = 1.06 μm) ~ 0.15 (λ = 10.6 μm)		91.03		[33]
	0.06 (λ = 3.39 μm, 150m) 0.35 (λ = 0.488 μm, 150m) 0.27 (0.488 μm, 800m)		4 9 11	λ = 0.488, 3.39 μm, diagonal path through beam, propagation distances indicated	[34]
$4 \cdot 10^{-10}$					[35]

$\sim 10^{-9}$	~ 0.14 (λ = 1.06 μm) ~ 0.16 (λ = 10.6 μm		4.4 1.1	Altering cross-angle,	[36]
$3 \cdot 10^{-9}$	0.5 (λ = 0.9 μm)		2		[30]
10^{-10}-10^{-11}					[31]
	0.06-0.18 (λ = 1.06 μm) 0.11-0.3 (λ = 0.53 μm)		6-35	Different aspect angles (ϕ = 90°, 45°,10°)	[8] [9]

In Table 5 experimental results on laser beam propagation through jet engine plumes reported in the literature are summarized. The magnitude of the reported values with respect to C_n^2 and beam wander agrees with those presented above.

5.2 Laser beam propagation in rocket plumes

Laser beam propagation through local zones of strong turbulence has been studied in plumes originating from rocket engines [37,38]. In this paragraph parts of the results from this work are reviewed. Two different types of rocket engines were investigated. The major difference between the two engines was the axial temperature. Although, the plume from solid fuel rocket engines differs from the plume associated with a jet engine with respect to flow characteristics, important information about the turbulence strength, scale lengths, beam broadening and correlation distances can be obtained from studies of rocket plumes. The study consisted of an experimental part and development of an appropriate turbulence model. The model was used to determine turbulence parameters such as e.g. the structure constant C_n^2 from the experimental data. A CFD code was utilised to calculate thermo-physical parameters i.e. temperature profiles, pressure, gas densities and gradients within the plume. The plume was studied experimentally using static and dynamic burning configurations. Only turbulence contributions from the plume were considered since all other effects were assumed to be several orders of magnitude lower in comparison to the plume.

5.2.1. Experimental set-up

Two different experimental configurations were utilised to study turbulence effects in plumes originating from rocket engines. In a static configuration the plume from the engine exhaust was directed vertically from ground as depicted in Figure 22A. Several laser diodes and photo detectors (x10) registered the signal perpendicular to the exhaust during burning of the engine. In addition, two diagonal paths (relative to the central axis of the plume) using a laser diode and a CO_2 laser were utilised. The laser diodes and corresponding receivers were placed in two vertical masts. The height of each mast was 28 m. The diode- and CO_2 lasers were pulsed using a pulse repetition rate (prf) about 2500 and 3000 Hz, respectively. The receivers were triggered on the onset of the rocket engine burn sequence. The gas velocity near the central flow axis was estimated to roughly 1000 m/s or higher. The signals from the detectors were recorded simultaneously and stored on a tape media. The on-axis temperature varies from approximately 2300 K close to the exhaust to 1000 K at the position of the highest located laser diode/receiver. Two different engine types were examined (type I and II). The major difference between the two types is the temperature

of the flowing gases. In addition to turbulence studies the extinction of the laser radiation during propagation through the plume was determined.

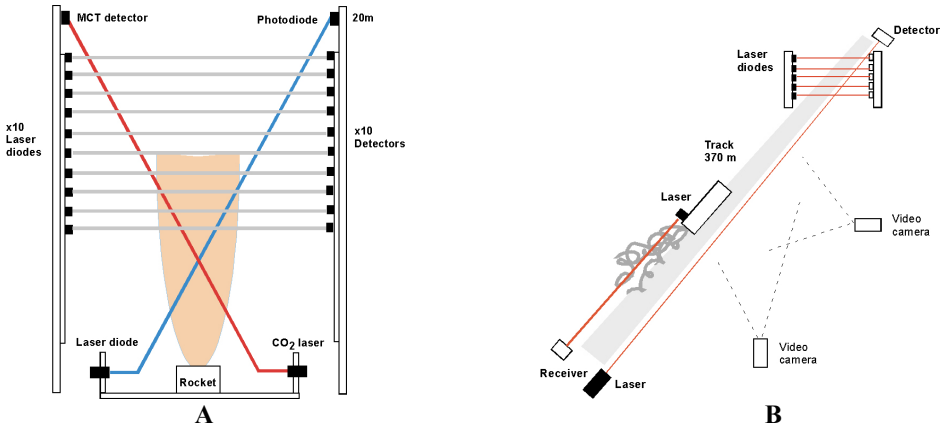

Figure 22 Experimental set up measuring perturbations during laser beam propagation in rocket plumes. A) Static set-up B) Dynamic set-up.

The temporal evolution of the plume turbulence from the rocket engine was studied using a 370 m long horizontal track (Figure 22B). In this study the rocket was mounted on a mobile unit and laser diodes were placed on the rocket and in several positions orthogonal to track at the end of the horizontal path. The laser diodes mounted on the rocket and at the start position measured the turbulence effects parallel to the moving rocket. Two video cameras were used to monitor the motion of the rocket.

5.2.2. Experimental results

During burning of the rocket engines signals were recorded on all channels in order to gather information about the turbulence effects at different positions relative to the location of the exhaust. In this paragraph only representative values of the turbulence (order of magnitude) parameters are discussed due to the large amount of experimental data. The data discussed was extracted from a channel with a location 7.6 m above the engine exhaust. An example showing the signal registered during burning of the engine is depicted in Figure 23. The signal exhibits strong fluctuations present up approximately 1.5 s after ignition of the engine. A decrease in the average signal can be observed during the first phase of the burning period.

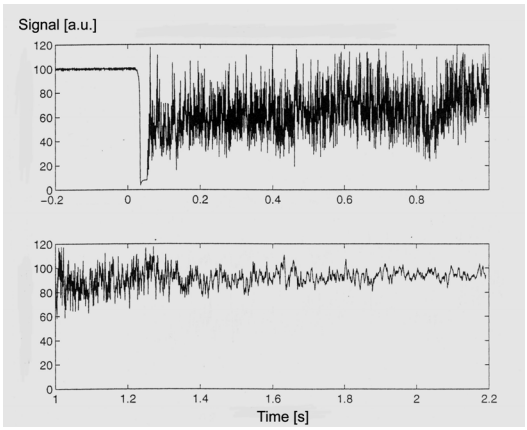

Figure 23 Signal registered during burning of the rocket engine. The time scale of the trace is divided into two separate graphs.

The signal observed during the burn sequence varied between 30 to 120% of the initial signal (no turbulence). The difference between the maximum and minimum registered signal is shown in Figure 24A. The most intense fluctuations diminish after approximately 1 s. The burning time for the engines was about 0.9 s. Strong intensity fluctuations can be observed during the initial burning phase and the standard deviation, σ_{lnI}, decreases from 0.12 to 0.02 in the time interval 0.1 to 0.2 s. No saturation effects were observed. The scintillation successively decreased and reached a level below 0.05 after 1 s (Figure 24B).

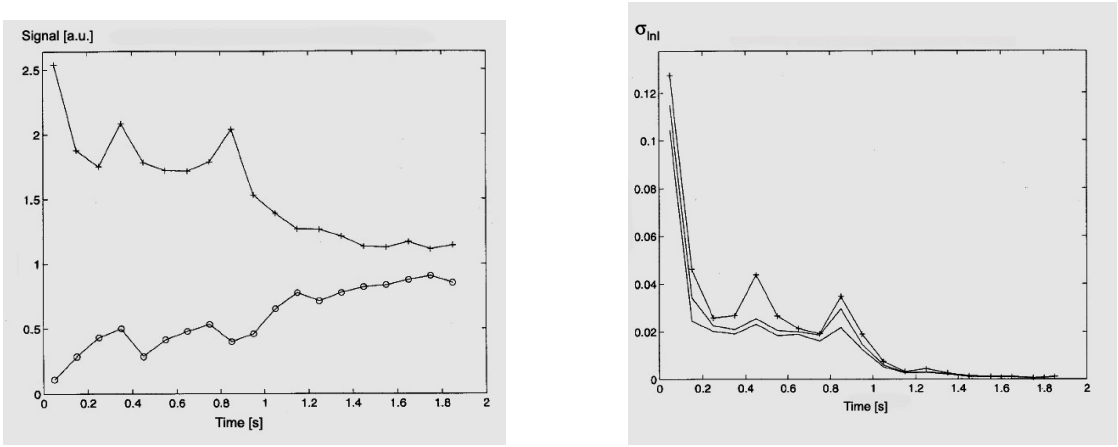

A **B**

Figure 24 A) Variation of the detector signal (max/min) during burning of a rocket engine. The maximum (upper trace) and the minimum detector signal (lower trace) are plotted. B) Log-irradiance standard deviation as a function of time.

The extinction of the laser radiation increased at closer distances to the engine exhaust. Summarizing the extinction results a transmission varying from 4 to 70 % was obtained. The coherence length during burning of the engine varied from sub-mm scale up to 20 cm after 1.5 s from the initiation of the engine (Figure 25A).

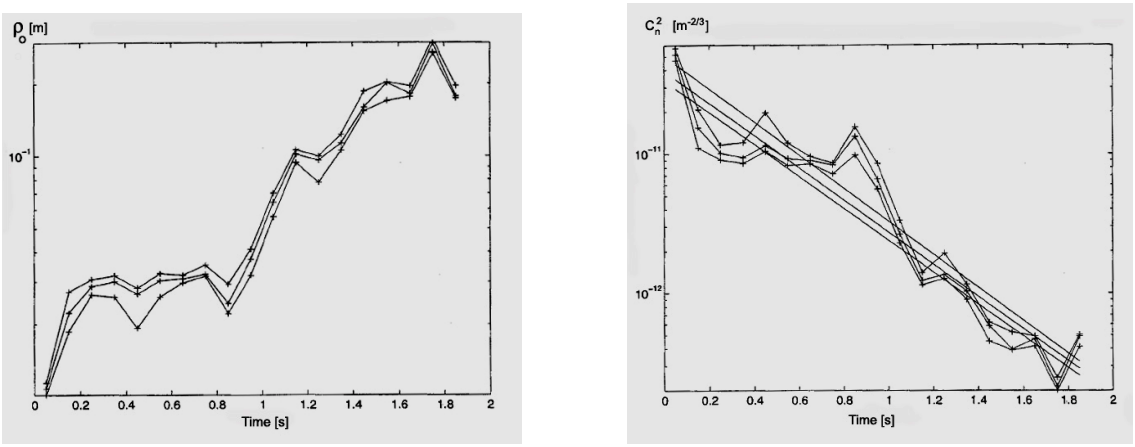

Figure 25 A) Variation in coherence length as a function of time. B) Variation of the structure parameter, C_n^2, as a function of time. The non-fluctuating lines denote results from the model described in the paragraph below.

The structure parameter derived from the experimental study is depicted in Figure 25B. The highest value was observed after ignition of the engine when the plume was developed. The C_n^2 fluctuates during the burn sequence and an overall linear decrease ranging from ~$5\cdot10^{-11}$ to $8\cdot10^{-12}$ $m^{-2/3}$ is illustrated in the example given in Figure 25B. The strongest observed turbulence strength corresponded to, $C_n^2 \approx 1.5\cdot10^{-9}$ and $1.5\cdot10^{-10}$ $m^{-2/3}$, for engine II and I, respectively. The structure parameter was derived using results from the calculations and experimental data. Turbulence parameters representative for the results obtained by studying laser beam propagation through rocket plumes are presented in Table 6. An outer scale length, L_o = 100 and 70 cm, and inner scale length, l_o = 2.6 and 0.5 mm was observed for the different engines. In Figure 25A, is an example showing how the coherence length varies as a function of the rocket engine burn time depicted. The coherence length, ρ_o, increases from approximately 5 mm to above 10 cm after 1.4 s burn time.

Table 6 Turbulence parameters attributed to laser beam propagation through rocket plumes

Engine	C_n^2 [$m^{-2/3}$] Experiment	C_n^2 [$m^{-2/3}$] Model	L_o [m] Outer scale	l_o [m] Inner scale
Type I	$1.5\cdot10^{-10}$	$2.3\cdot10^{-10}$	$100\cdot10^{-2}$	$2.6\cdot10^{-3}$
Type II	$1.5\cdot10^{-9}$	$2\cdot10^{-9}$	$70\cdot10^{-3}$	$0.5\cdot10^{-3}$

5.2.3. Modelling turbulence in rocket engine plumes

The purpose of this paragraph is to describe a method that can be utilized to calculate parameters (order of magnitude) describing the turbulence in a rocket engine plume. In particular the structure parameter and beam broadening effects are of interest. By studying the structure function and assuming slowly varying means the following expression can be derived as a first approximation

$$D(r,r') \approx \left\langle \left(\Delta n(r) - \Delta n(r')\right)^2 \right\rangle \qquad \text{eq. 31}$$

where *Δn(r)* denotes a small fluctuating part of the reflective index. According to Kolmogorov theory the structure can be expressed in terms of C_n^2

$D_n(\rho) = C_n^2 \rho^{\frac{2}{3}}$ if $l_o << \sqrt{\lambda L} << L_o$.

Assuming $\rho = L_o$ the structure function can be expressed as

$$C_n^2 \approx 2\sigma_n^2 L_o^{-\frac{2}{3}} \quad \text{eq. 32}$$

where σ_n^2 is the variance of the reflective index fluctuations. The relation between the fluctuations in refractive index can be correlated to the alterations in the temperature by the using the relation

$$\sigma_n^2 = \sigma_T^2 \left|\frac{\partial n}{\partial T}\right|^2 \quad \text{eq. 33}$$

Inserting eq. 33 into eq. 32 the structure parameter can be expressed as

$$C_n^2 \approx 2\sigma_T^2 \left|\frac{\partial n}{\partial T}\right|^2 L_o^{-\frac{2}{3}} \quad \text{eq. 34}$$

where σ_T^2 is the temperature variance in the plume, $\left|\frac{\partial n}{\partial T}\right|^2$ is the temperature gradients of the refractive index and L_o is the outer scale length. The temperature gradient of the refractive index can be derived according to

$$\frac{\partial n}{\partial T} = -83.3 \cdot 10^{-6} \frac{p}{T^2} \quad \text{eq. 35}$$

where p is the gas pressure and T the temperature. The outer length scale can be approximated as $L_o \approx y_{0.5U_c}$ where $y_{0.5U_c}$ is the distance corresponding to one half of the axial gas velocity (U_c) within the plume. Finally, the temperature variance within the plume needs to be estimated using results described in ref. [39] According to Chen and Rodi can the temperature variance for turbulent buoyant jet be approximated by

$$\sigma_T^2 \approx K \cdot \Delta T^2 = K(T_c - T_a) \quad \text{eq. 36}$$

where T_c is the axial gas temperature, T_a the ambient temperature outside the plume and K a constant fitted to experimental data. Using the expression derived in eq. 34 to eq. 37 the outputs from CFD calculations provide all necessary parameters for calculating the structure parameter. A numerical example is presented to verify the consistency of the model. In order to estimate C_n^2 the following parameter values are assumed: T_c = 800 K, T_a = 300 K, L_o = 0.3 m, K ≈ 0.2 and $\left|\frac{\partial n}{\partial T}\right| \approx 1.5 \cdot 10^{-7}$ K^{-1} resulting in a structure parameter $C_n^2 = 5 \cdot 10^{-9}$ m$^{-2/3}$. Hence, the simple model described above predicts the same order of

magnitude as the experimentally observed results. By using CFD results variations of C_n^2 within the plume can be estimated.

6. DISCUSSION AND CONCLUSION

Strong perturbations of the optical field may cause significant performance degradation of an airborne laser countermeasure system. The phenomena discussed in this report originates from aero-optical effects due to the flow-field around the platform fuselage and turbulence effects occurring close the jet engine exhaust plume. The purpose of the report was to make estimates of the order of magnitude of these phenomena considering a DIRCM application and survey the data available. Corrections of a perturbed optical field may be provided by implementation of adaptive optics. However, the achievable amount of correction of an aberrated laser beam depends on several factors such as e.g. the strength of the perturbation, scale size and the temporal spectrum. Strong beam perturbation theory is complicated and numerical techniques must often be used to obtain reliable results. In this report the use of simple analytical formulas was emphasized to in order to estimate the effects. For the power in bucket calculations and tracking accuracy a more detailed analysis was performed.

The atmospheric turbulence phenomena have been studied in detail during the last thirty years and the characteristic features are well known. Comprehensive theoretical models have been developed under weak and moderate turbulence conditions. In the strong perturbation region often heuristic and asymptotic theories are utilised to calculate laser beam properties. Hitherto, models valid for all turbulence strengths have been lacking. Considering the atmospheric turbulence situation present in DIRCM scenarios the effects present at higher altitude (above 1 km) can probably be neglected as a first approximation in comparison to other beam degradation sources. The platform induced jitter and perturbations from the plume give a larger contribution to the beam degradation effects. At high altitude vary the C_n^2 in the range 10^{-16} to 10^{-17} $m^{-2/3}$, which cause small scintillation effects at shorter ranges i.e. ~3 km in the DIRCM case. At longer ranges of engagement the accumulated phase distortions of the wave front may give rise to stronger scintillations. One important issue to emphasize is the temporal variation of the signal. This includes both the retro reflected and the intensity in front of the seeker aperture. The high velocity of the FJ platform (300-600 m/s) implies high temporal frequency. If the beam is directed perpendicular to the moving direction this frequency can be of the order 1 to 5 kHz. To first order the reduction in power in bucket due to beam broadening only needs to be included for the atmospheric contribution. Studying the low altitude scenario occurring during landing or take-off typical C_n^2 values are 10^{-14} to 10^{-15} $m^{-2/3}$. More attention on the atmospheric turbulence is required in this case.

Considering the discussion on AO-effects in the case of a DIRCM transmitter located on a fast jet the conclusion is that these effects can probably be neglected at wavelengths in the mid-ir. The effects from the boundary layer turbulence are most severe. The estimates presented above suggest only minor degradation on the beam quality for the sub-sonic low altitude and the super-sonic high altitude cases. Strehl ratios, $S = 0.5 - 0.9$, can be acceptable for the DIRCM application. It should be noted that the worst cases occurs when the beam is directed along the aircraft body. Inviscid flow and shock contributions can also be managed with appropriate design of the DIRCM turret. In the third scenario a shorter wavelength is used for the laser transmitter that may necessitate a more thorough investigation of the aero-optical phenomena. This fact was clearly evident in the calculations using a wavelength, $\lambda = 1.0$ μm, where a considerable reduction in Strehl was obtained ($S < 0.1$ for several sub-sonic cases at ground level). Accordingly, a more detailed analysis is required for the air-to-ground targeting scenario.

The ability to direct the laser beam in close vicinity, or even trough the plume from the jet engine may require compensation methods to retain the beam quality and reduce the beam jitter. The strong turbulence present in the plume degrades the beam quality considerably. Pointing the beam through, or close the

exhaust, should be avoided. Several of the threat scenarios in the DIRCM engagement do not necessitate an ability to direct the beam through the plume. The critical case occurs close to landing, or take-off, if a SAM missile is fired aft of the aircraft. In this case the turbulence from the exhaust affects the beam. Since scales of the turbulence are small and the temporal frequencies very high order adaptive optics compensation of plume effects is a very delicate task. The beam wander, which occurs on a slower time scale, may be partly corrected for by a fast tip-tilt sensor.

Model calculations were carried out in order to estimate the influence from phenomena associated with AO and the turbulence effects in the plume. These models provide information about the order of magnitudes of the different phenomena. Accurate CFD calculations need to be carried out for detailed analysis of phenomena discussed in this report. Considering AO and plume turbulence effects numerical methods exist to calculate the properties of the flow field. However, detailed knowledge about environmental parameters is required for such calculations. Using the output from CFD models properties of optical propagation through the flow field can be derived.

In this paragraph we outline some proposals for further work in this field in order to obtain a deeper understanding of the limitations and capabilities of DIRCM systems:

- Considering jet engine plumes a more accurate model needs to be developed and verified against field experiments studying turbulence characteristics in plumes. The experiments can be performed with the aircraft tethered to ground. Of particular interest are the turbulence effects close to the plume.

- An improved model is to use CFD calculations to derive the complete 3D field of index of refraction fluctuations. In this case CFD calculations of the flow field need to be combined with appropriate propagation models.

- Development of a phase screen turbulence model valid for laser beam propagation in exhaust plumes.

- Experimental and theoretical studies of methods able to compensate for system performance degradation. This includes low-order adaptive optics methods.

7. APPENDIX – TRACKING OPTIMISATION USING SIGNAL STATISTICS

This appendix summarises results concerning performance of laser detection, tracking and power in bucket calculations. The detection probability of a missile target in high and low signal levels is investigated. Tracking accuracy is also studied and how the tracking accuracy is influenced by turbulence, mechanical jitter and mean signal to noise ratio (SNR). Finally, power in bucket is calculated as a function of the jitter and turbulence strength. An important performance parameter is the beam size in relation to the beam jitter.

7.1 Detection.

An optimum beam size can be obtained for a given detection probability P_d, false alarm probability P_{fa} and detection technique (direct or coherent detection). The optimum beam size can be characterised by the ratio

$$\alpha = \frac{\mathrm{w}}{\sigma_{\mathrm{j}}} \qquad \text{eq. 37}$$

where w is the beam vacuum radius at the target and σ_j is the standard deviation of the beam jitter. If the beam radius is too large the *SNR* will be reduced resulting in a lower P_d and higher P_{fa} value. On the other hand, if the beam is too narrow the jitter will influence the detection probability and false alarm in a negative way. Therefore an optimum value of beam spread vs. the beam jitter i.e. an optimum α value is expected. It is assumed that the seeker aperture is smaller then the beam width for relevant ranges and can be considered as a point target. Direct detection is treated in this work.

Consider detection of the returned laser beam from the target and a signal current i_s, threshold current i_T and a noise current i_n. Assuming a gaussian noise distribution the expressions for the detection probability $P_d(i_s)$ and the false alarm probability P_{fa} are given by:

$$P_d(i_s) = \frac{1}{\sqrt{2\pi\overline{i_n^2}}} \int_{i_T - i_s}^{\infty} \exp(-i^2 / 2\overline{i_n^2}) di = 1/2 \cdot [1 + erf((i_T - i_s)/\sqrt{2\overline{i_n^2}})] \qquad \text{eq. 38}$$

and

$$P_{fa}(i_T) = \frac{1}{\sqrt{2\pi\overline{i_n^2}}} \int_{i_T}^{\infty} \exp(-i^2 / 2\overline{i_n^2}) di = 1/2 \cdot [1 - erf(i_T / \sqrt{2\overline{i_n^2}})] \qquad \text{eq. 39}$$

7.1.1. Strong glint

We also assume a strong signal return with constant amplitude. Knowing the probability density function (pdf) for the detection probability and for the intensity (or current distribution) the detection probability averaged over all possible intensities can be computed as

$$P_d = \int_0^{\infty} P_d(i) \cdot P_I(i) di \qquad \text{eq. 40}$$

Probability density functions and other relevant formulas can be found in the monograph by Andrew and Phillips[2].

7.1.2. Calculation of detection probabilities P_d for different probability density functions

The influence of the turbulence levels for different beam parameters $\beta = \alpha^2$. Figure 26 shows the required SNR to fulfil a detection probability of PD = 90% at a false alarm level $P_{fa} = 10^{-6}$. The SNR increases with the beam width (measured by β for a constant residual jitter) and with turbulence strength expressed in terms of the log intensity variance σ^2_{lnI}. We can also deduce the optimal beam to jitter ratios (β or α) for different SNR and detection probabilities in presence of weak turbulence. Figure 27 shows an example of how the surface *Pd (-Log(Pfa) ,β)* looks like. For weak turbulence ($\sigma^2_{lnI} = 10^{-6}$) the case is nearly identical for the case when no turbulence is present. If the turbulence level is increased, $\sigma^2_{lnI} = 0.1$ (weak turbulence guilty for $\sigma^2_{lnI} < 0.5$) the probability is reduced for a wider range of false alarm probabilities and beam jitter β.

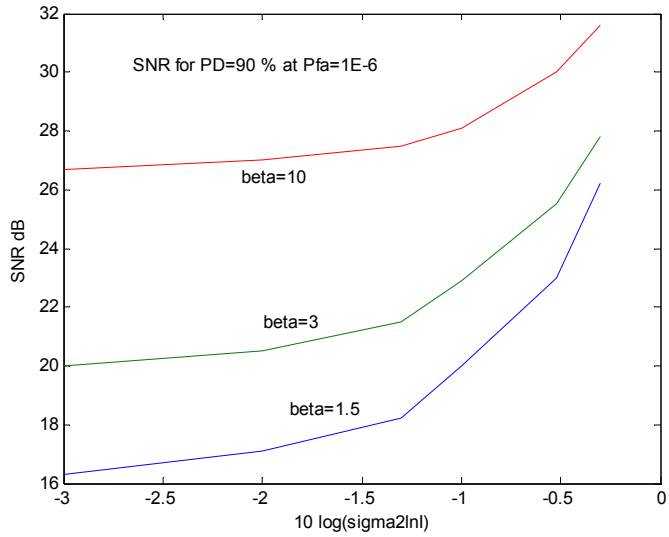

Figure 26. The SNR needed for a detection probability PD = 90 % at a false probability $P_{fa}=10^{-6}$ with different turbulence levels (σ^2_{lnI}) and beam jitter (β).

Considering jitter we can from Figure 27 discern that there exist an optimum value for the beam size relative to the beam jitter, which has the lowest P_{fa} for a given P_D. This becomes clearer when plotting the contour for P_D vs. β and P_{fa} as shown in Figure 28. Higher turbulence results in a lower optimum α meaning that we need a narrower beam relative to the beam jitter to obtain optimum (lowest P_{fa}) conditions. Note that a given SNR for the no jitter case, $\alpha = 1$ and that changing the α for a given jitter value means scaling the SNR as $SNR(\alpha) = SNR/\alpha^2$.

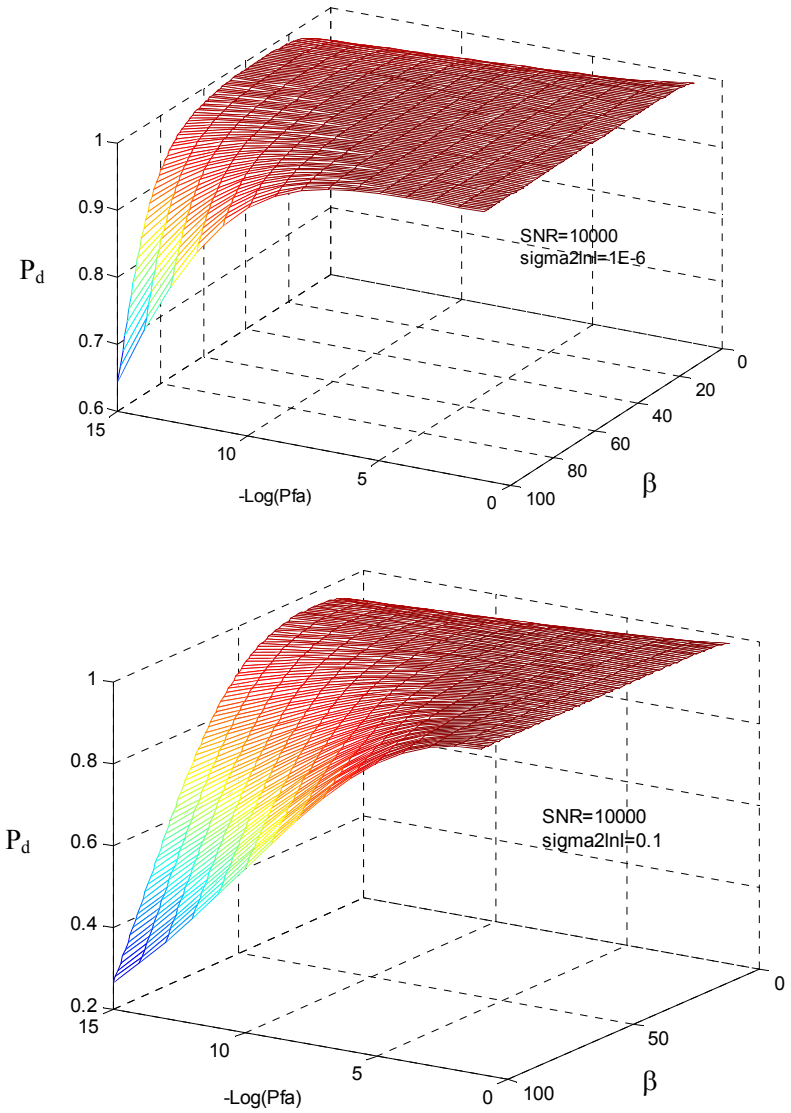

Figure 27. The detection probability *Pd* as a function of the jitter parameter β and the false alarm rate (measured as $-\log(P_{fa})$. SNR = 40 dB and weak turbulence ($\sigma^2_{lnI} = 10^{-6}$ and 0.1 respectively) was assumed.

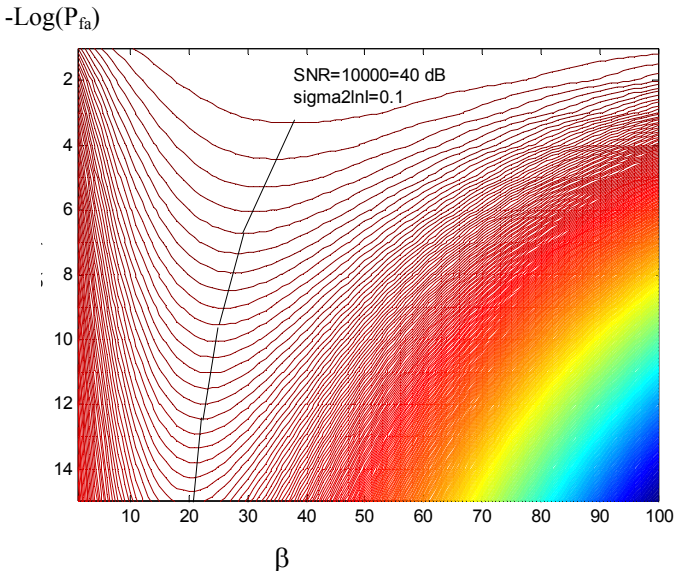

Figure 28. Contour plot for the detection probability *Pd* vs. the jitter parameter β and the false alarm probability showing optimum beam sizes vs. jitter for different *Pd*. Weak turbulence ($\sigma^2_{lnI} = 0.1$).

Figure 29 shows optimal α for detection in weak turbulence plus jitter and the corresponding detection probability for a SNR =40 dB (without jitter). A larger turbulence level leads to a smaller optimum beam relative to σ_j.

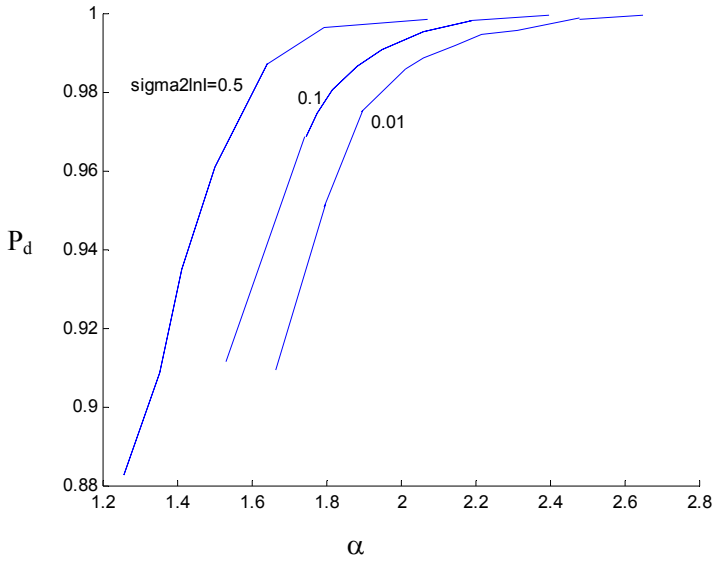

Figure 29. Optimal α (with respect to lowest P_{fa}) for detection in weak turbulence plus jitter and the corresponding detection probability for a SNR =40 dB(no jitter)

In Figure 30 the detection probability and optimal α values for a nominal SNR = 30 dB is depicted. For a given detection probability the strong turbulence case ($\sigma^2_{lnI} = 0.5$) means a larger beam relative to the jitter. For a given beam the strong turbulence means a lower *Pd* as expected. In the low turbulence region a larger α mean a slightly increased detection probability for a given beam to jitter ratio, which might be

explained by the fact that weak turbulence increases the probability for a higher irradiance compensating the jitter loss.

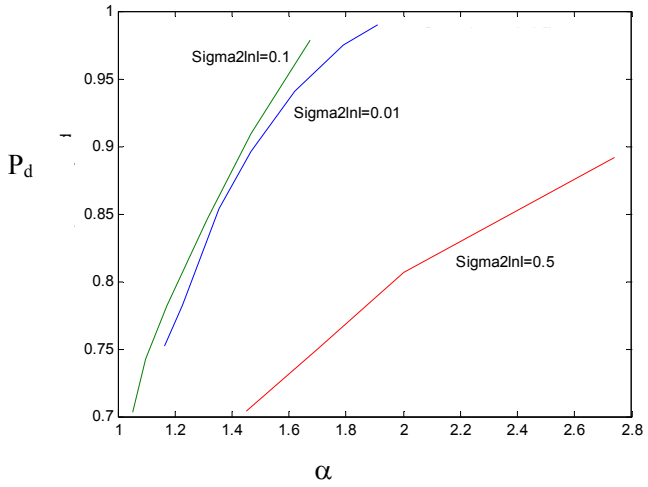

Figure 30. Probability of detection vs optimal α for a nominal SNR = 30 dB.

Strong turbulence and jitter

In this case examples of pdf's and detection probabilities in the presence of strong turbulence are presented. An exponential pdf was used to characterise strong scintillations. Figure 31 shows the detection probability for a given false alarm $P_{fa} = 10^{-6}$ and for different beta assuming a given $< I > = 1$ for the turbulence exponential pdf. A relative weak dependence regarding beam jitter on the detection probability in presence of strong turbulence can be observed.

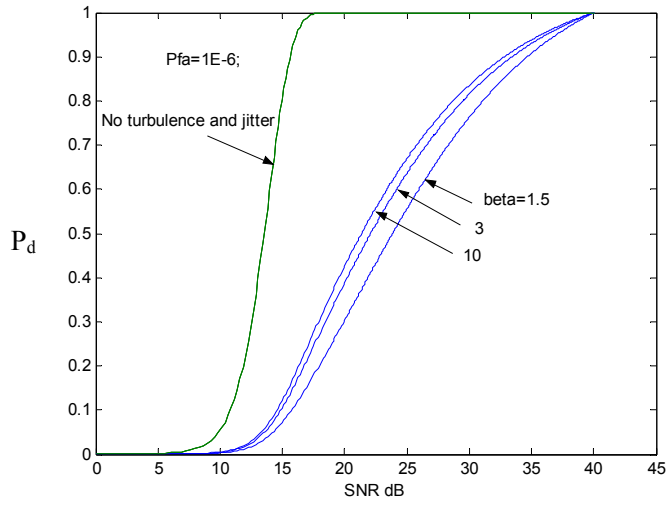

Figure 31. Total detection probability vs. SNR for different β in presence of strong turbulence and jitter.

The Gamma-gamma pdf

Recently Habash et al. developed a model for the pdf of an optical beam in a turbulent medium covering both the single- and the double-path cases[40]. The model is a two-parameter distribution based on a doubly stochastic theory combining small-scale irradiance fluctuations (mainly scintillations) with larger scale fluctuations (mainly beam wander), both governed by independent gamma distributions. The resulting pdf is a generalized k-distribution which the authors denotes the gamma-gamma pdf. The model has shown good agreement with experimental data. It is assumed that the irradiance, I, can be modelled as $I = x * y$ where x arises from the large scale turbulent eddies and y from the small scale ones.

The Rytov variance parameter is defined as $\sigma_I^2 = 1.23 \cdot C_n^2 \cdot k^{7/6} \cdot L^{11/6}$. I Figure 32 the gamma-gamma pdf with the Rytov variance as a parameter has been plotted. The difference between the gamma-gamma pdf and the lognormal pdf is more pronounced for high turbulence levels, as can be seen in Figure 33.

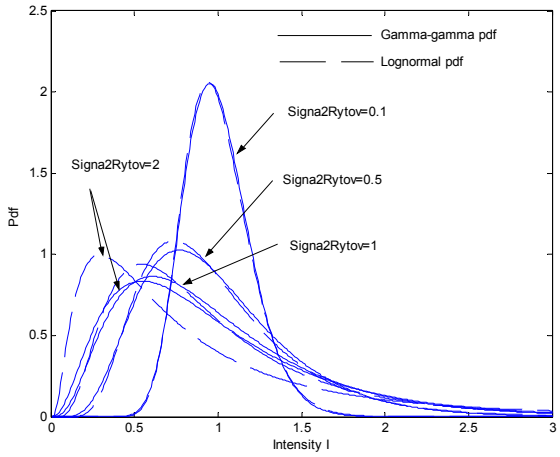

Figure 32. Comparison between the lognormal and the gamma–gamma pdf vs. different turbulence levels indicated by the Rytov variance.

The probability of exceeding threshold vs. the threshold I_t is plotted in Figure 33 for the gamma-gamma pdf and different Rytov variances including a comparison with the corresponding result for a lognormal pdf. The difference is marginal except for Rytov variance larger than about 0.5.

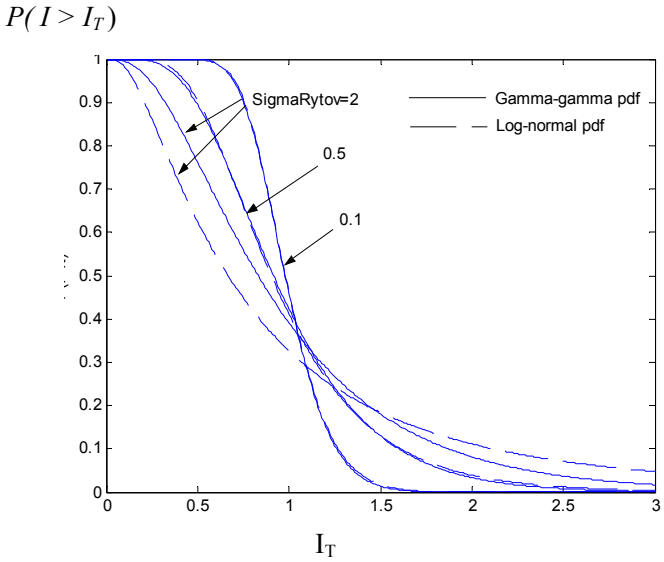

Figure 33. The probability of exceeding a threshold for a gamma-gamma pdf at different levels of the Rytov variance compared wit that from a lognormal pdf.

7.2 Power in bucket optimization

For the DIRCM application the power in bucket at the target is a parameter of importance. If the probability density for jitter and turbulence is known the probability that the intensity exceeds a given threshold I_{min} can be derived. Some selected results covering jitter only, weak turbulence and jitter and strong turbulence and jitter using the gamma-gamma pdf are presented.

Weak turbulence and jitter

In Figure 34 we have plotted the probability to exceed the threshold I_{min} for weak turbulence and jitter, assuming $\sigma^2_{lnI} = 0.05$ vs the intensity I uncompensated (upper) and compensated for the beam size change by the change of α. We can see that low probabilities to exceed threshold for the "absolute" intensity the small beam vs. jitter (low α) gives a higher I_{min} but that this is change for high probabilities, see figure 49.

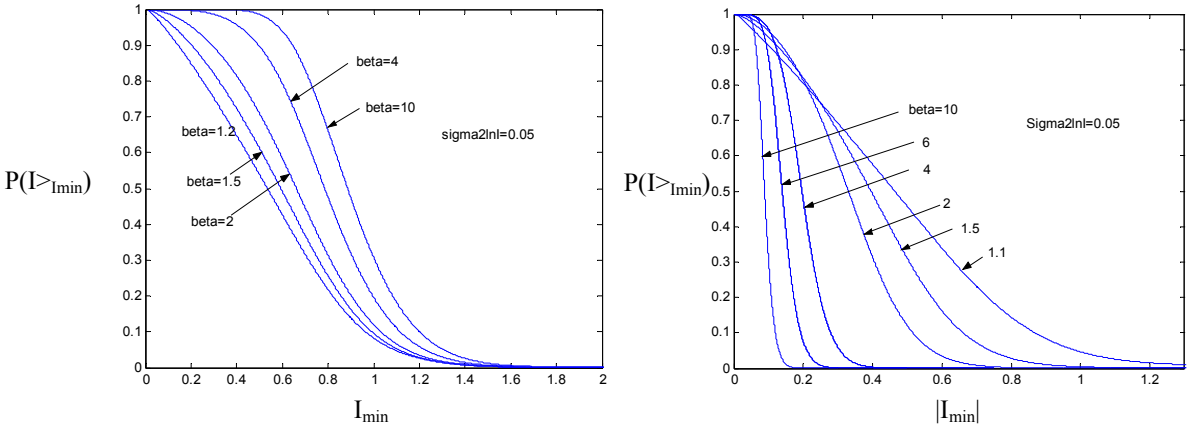

Figure 34. Probability to exceed a given intensity threshold P($I>I_{min}$) for different beam size to jitter ratio α.. In the left figure the "absolute" intensity means that we are scaling the intensity with the beam size as $I(\alpha) = 1/\alpha^2$. The turbulence level was $\sigma^2_{lnI} = 0.05$.

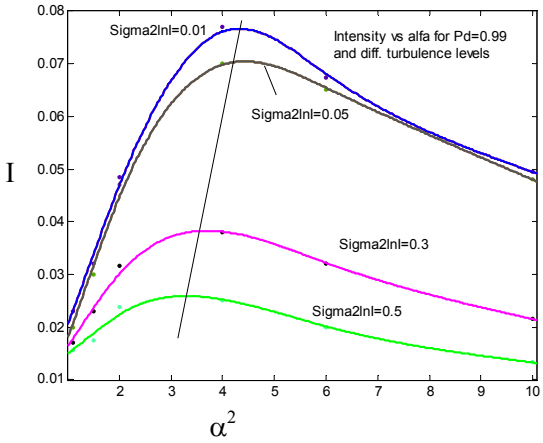

Figure 35. Absolute intensity (scaled with α) vs α and Pd(I>Imin) = 0.99. Different turbulence levels are indicated by σ^2_{lnI}.

In Figure 35 the absolute intensity vs, α and different turbulence are shown. As can be observed the increasing turbulence strength lead to a lower optimal α value (smaller beam vs. jitter) and a lower absolute intensity value.

Strong turbulence and jitter

In a direct analogy to the weak turbulence case the similar calculations were carried out for strong turbulence and jitter. The relative influence of α is reduced in strong turbulence, as one should expect.

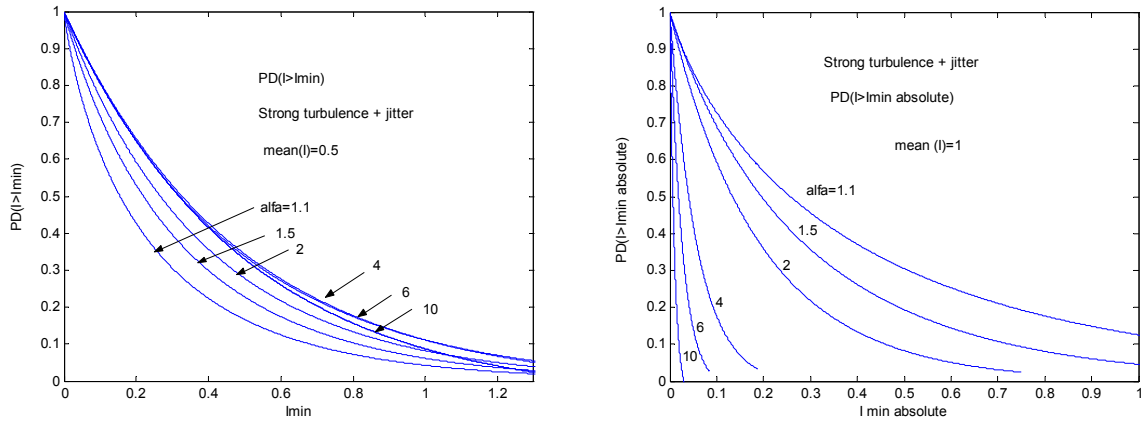

Figure 36. The probability for $I>I_{min}$ in strong turbulence and jitter. The mean refer to the mean in the exponential pdf describing the scintillation. Lower figure shows the probability against absolute intensity (compensated for change in α).

As observed in Figure 36 the strong turbulence case does not lead to an optimum beam parameter α, instead the smaller α the better (higher threshold I_{min}). Figure 36 refers to the probability of exceeding the threshold = 0.99.

The gamma-gamma pdf.

In Figure 37 we have plotted the threshold intensity for 90% (left) and 99 % (right) exceeding probability vs the beam parameter α. The optimum α values range from 1.3 - 1.6 for the 90 % case and 1.8 - 2.1 for the 99 % case**.** Figure 38 shows the optimal thresholds obtained from optimal beam size to jitter ratios (from Figure 37) resulting in 90 and 99 % exceeding probability vs. the turbulence level given as the Rytov variance.

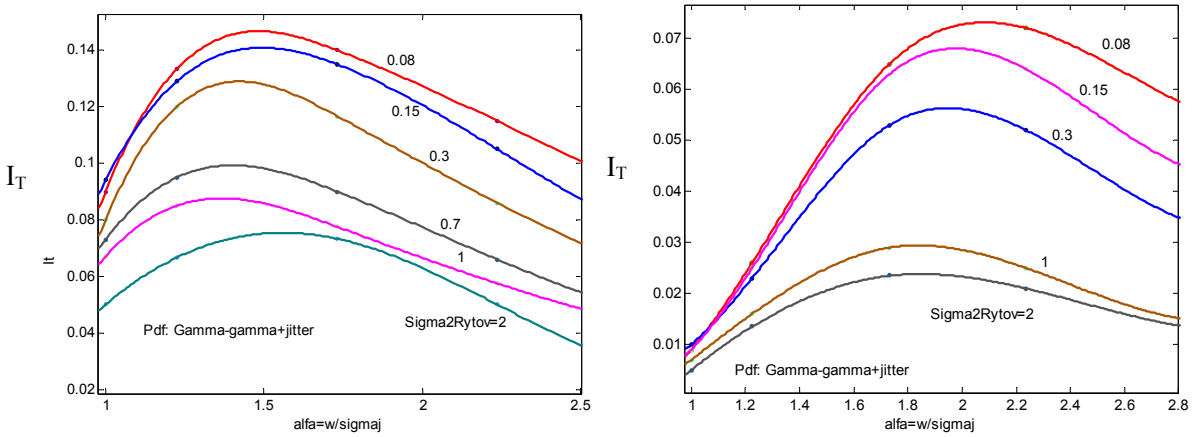

Figure 37. *The threshold intensity for 90% (top) and 99 % (bottom) exceeding probability vs the beam parameter α. The optimum alfa values range from 1.3-1.6 for the 90 % case and 1.8-2.1 for the 99 % case.*

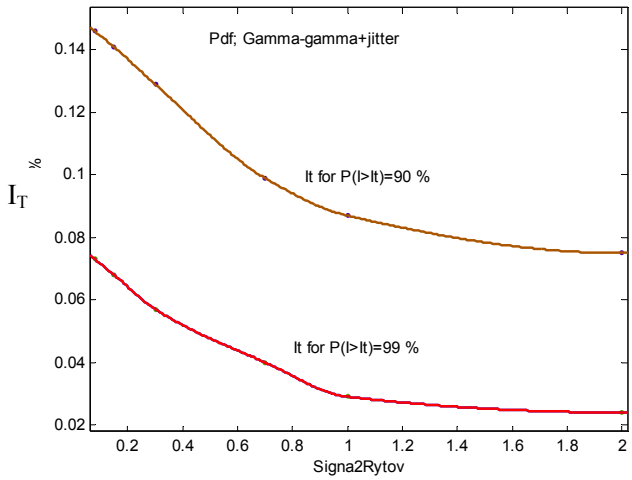

Figure 38. *The optimal thresholds obtained from optimal beam size to jitter ratios (from Figure 37) resulting in 90 and 99 % exceeding probability vs. the turbulence level given as the Rytov variance.*

7.3 Tracking performance

Often the rms error σ for the angle in an imaging tracking system is written as:

$$\sigma = \frac{g(\theta_S)}{SNR_I} \qquad \text{eq. 41}$$

where g is some function (often approximated by a constant /θ_S for the region of interest) of the image spot θ_S (in radians) and SNR_I the signal to noise ratio (current) in the tracking system bandwidth. The task is to investigate how this expression applies for turbulence scintillations and mechanical beam jitter.

Low signal limit.

Maximum Likelihood Estimate (MLE) for a fading target with no noise.

We start with the low photon counting regime, which might be relevant for small returns, for example if the retro reflex is blocked, and only the surface reflex from the dome or from other components in the seeker. Following Elbaum et al. an expression for the angular error as a function of mean signal count with the target fluctuation as a parameter can be derived [41]. Figure 16 shows the RMS error for the MLE estimate vs. mean signal photon count for different mean signal photon count. We have assumed the angular target position to be ¼ of the spot size i.e. $\theta = 1/4 \cdot \theta_S$.

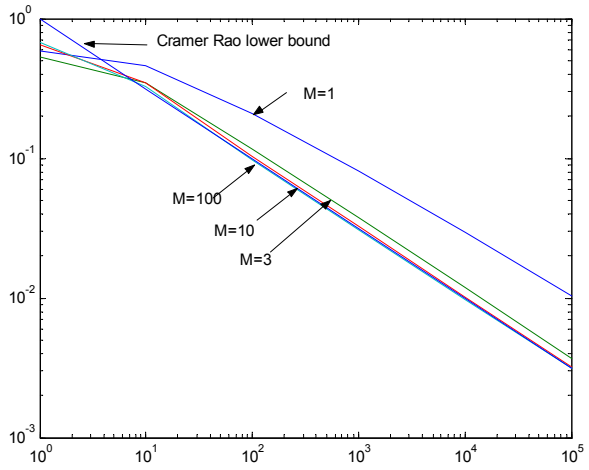

Figure 39. RMS error for the MLE estimate vs. mean signal photon count for different mean signal photon count. It was assumed that $\theta = 1/4*\theta_S$ i.e. the angular target position was ¼ of the spot size.

MLE for a fading target with weak noise.

The estimate rms error is target-fading limited for large signals, as one should expect. This is illustrated in Figure 40. NN denotes the mean noise counts and NS the signal counts. M is the number of freedoms for the signal statistics assuming a gamma function for the pdf. M = 1 then gives an exponential distribution

characteristic for a fully developed speckle. The “slow AGC” approximation means the automatic gain control in the detector is slow. In this case this is interpreted as that the sum in the dominator is replaced with the mean sum.

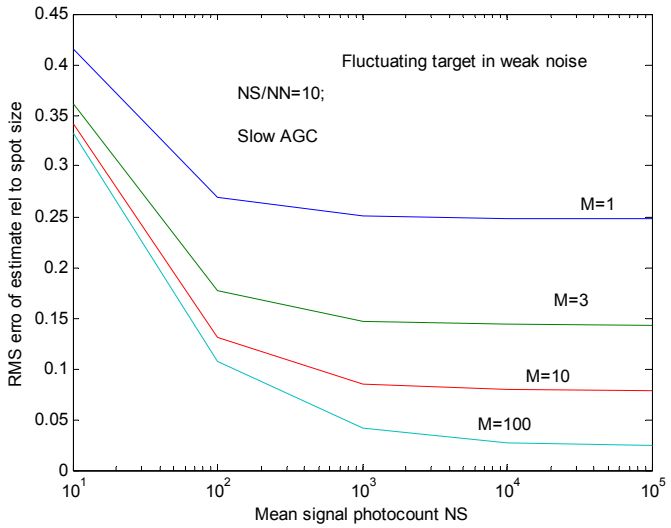

Figure 40. Rms error for angle estimate for a fluctuating target in weak noise. Slow AGC approximation was assumed. The rms error is target fluctuation limited for large signal levels.

High signal regime

Simulation of tracking accuracy

For the general case of a certain signal and noise pdf it is hard to obtain analytical solutions for the mean and variances of the estimates. Therefore a number of numerical simulations have been carried out to illustrate that the pdf and SNR will affect the tracking accuracy. The gamma function was chosen as a first representation for the signal fluctuations in order to estimate the signal distribution influence on tracking performance.

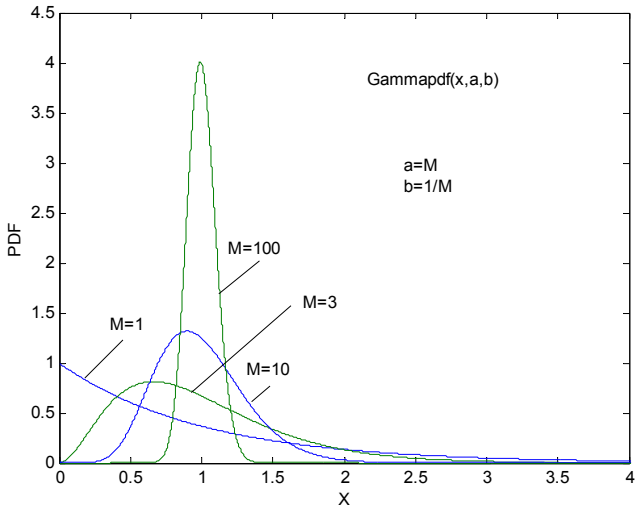

Figure 41. *Pdf used to simulate tracker performance. The negative exponential pdf (M=1) is indicative of very strong turbulence.*

The intensities in the left and right side of the quadrant detector used for the tracking is defined as $I_{1(2)}$. Then the ratio q is simulated as:

$$q = \frac{\theta}{\theta_S} = \frac{I_2 - I_1}{I_1 + I_2} \qquad \text{eq. 42}$$

using the gamma pdf. Detector noise can be added by using a gaussian pdf to represent $I_{1(2)}$. $I_{1(2)}$ are simulated as independent variables with the means $I_1 = k \cdot I$ and $I_2 = (1-k) \cdot I$. Figure 43shows the normalised rms error of the angular estimate for the signal obeying different pdf's represented for different M. Note the difference for strong turbulence and beam jitter represented by the negative exponential intensity distribution and the weak turbulence case represented by M = 10-100.

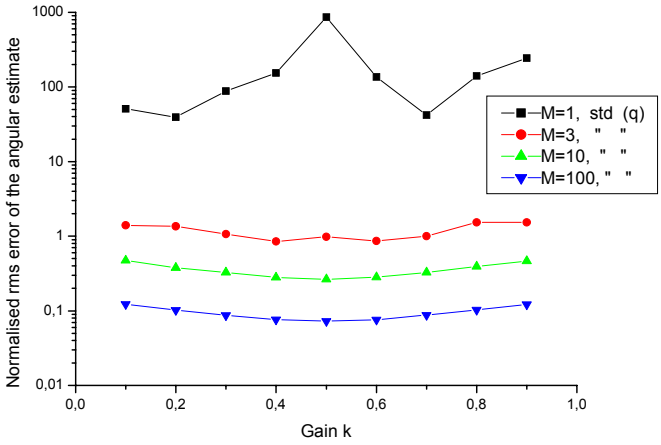

Figure 42. Normalised rms error of the angular estimate for the signal obeying different pdf's represented by different M. The diagram is based on the simulation of 10000 runs per point.

We would expect a better estimate, at least for strong signal fluctuations by allowing a slow AGC, that is taking the long term mean (in relation to the turbulence time constant) sum in the denominator in eq. 42.

This is shown in Figure 44 where the rms estimate is much lower, especially for the more fluctuating signal cases (lower M-values).

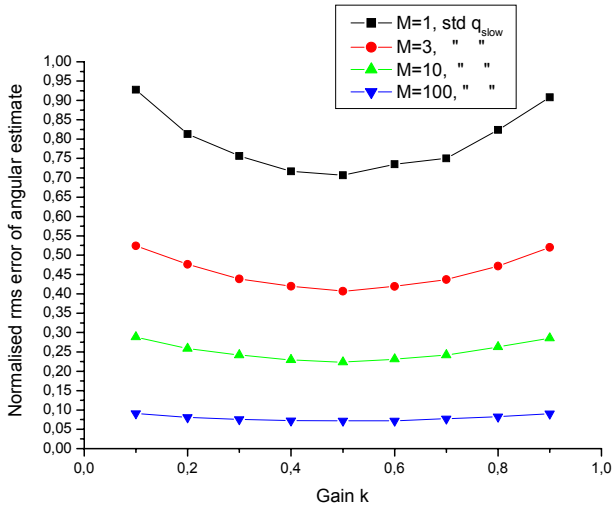

Figure 43. Normalised rms error of the angular estimate for the signal obeying different pdf's represented by different M. Slow AGC, that is the sum of the channel signals in the denominator of the tracking ration is replaced with a mean value. The diagram is based on the simulation of 10 000 runs per point.

We have also looked at the influence of detector noise assuming a zero mean gaussian noise distribution. In Figure 44 the normalized rms error is plotted for different M and with no noise in relation to SNR = 3 and 10 dB. As expected the gain of having a large SNR is less for a strong fluctuating target.

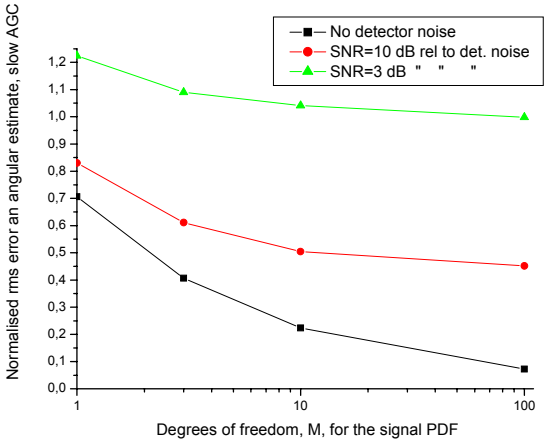

Figure 44. Normalized rms error for different M and with no noise in relation to SNR=3 and 10 dB. As expected the gain of having a large SNR is less for a strong fluctuating target.

Beam size optimisation in DIRCM systems with respect to tracking.

We have simulated a quadrant tracker performance assuming a target on bore sight. In Figure 45 and Figure 46 we show the normalized tracker error (normalized to the tracking system resolution given by the beam spot size in the quadrant detector plane. As can be seen the smaller the SNR the larger tracking error as expected. There exist an optimum beam size for which SNR = 10 is around $\alpha = 1.7$ and SNR = 30 is

around $\alpha = 2.3$. For SNR = 100 we find $\alpha_{opt} = 3.3$ and for SNR = 1000 we find $\alpha_{opt} = 5.7$. The SNR is scaled with α during the simulations. For each curve 100 simulations of the tracking ratio q has been performed using the assumption of the total signal amplitude being the sum of a signal in turbulence and jitter following the distribution given above with added Gaussian noise. Figure 47 shows the case for weak turbulence and tracking. For increasing turbulence the error increases and no clear optimum is found. This is especially true for strong turbulence according to Figure 48.

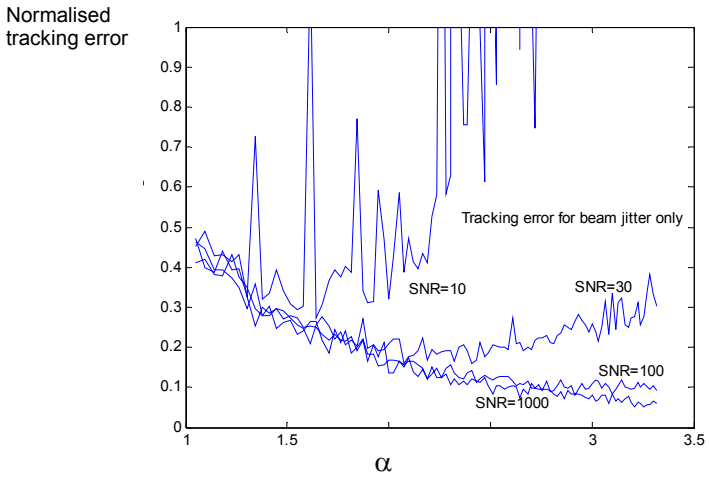

Figure 45. Normalised tracking error vs. α. Different nominal SNR (without jitter) are given in the figure.

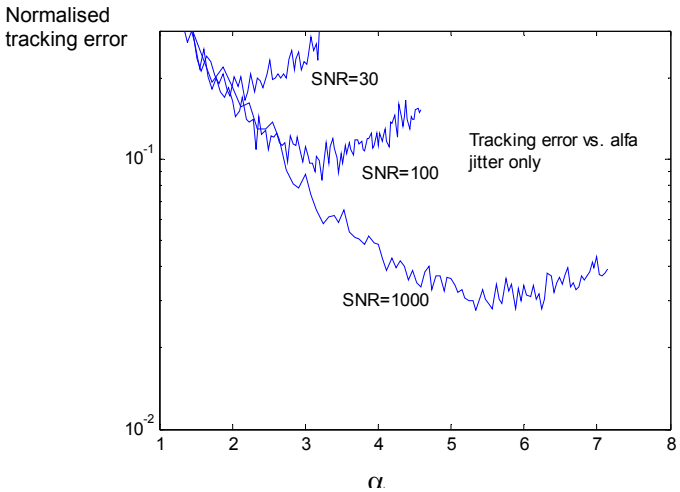

Figure 46. Same as Figure 47 but enlarged and logarithmic in error axis.

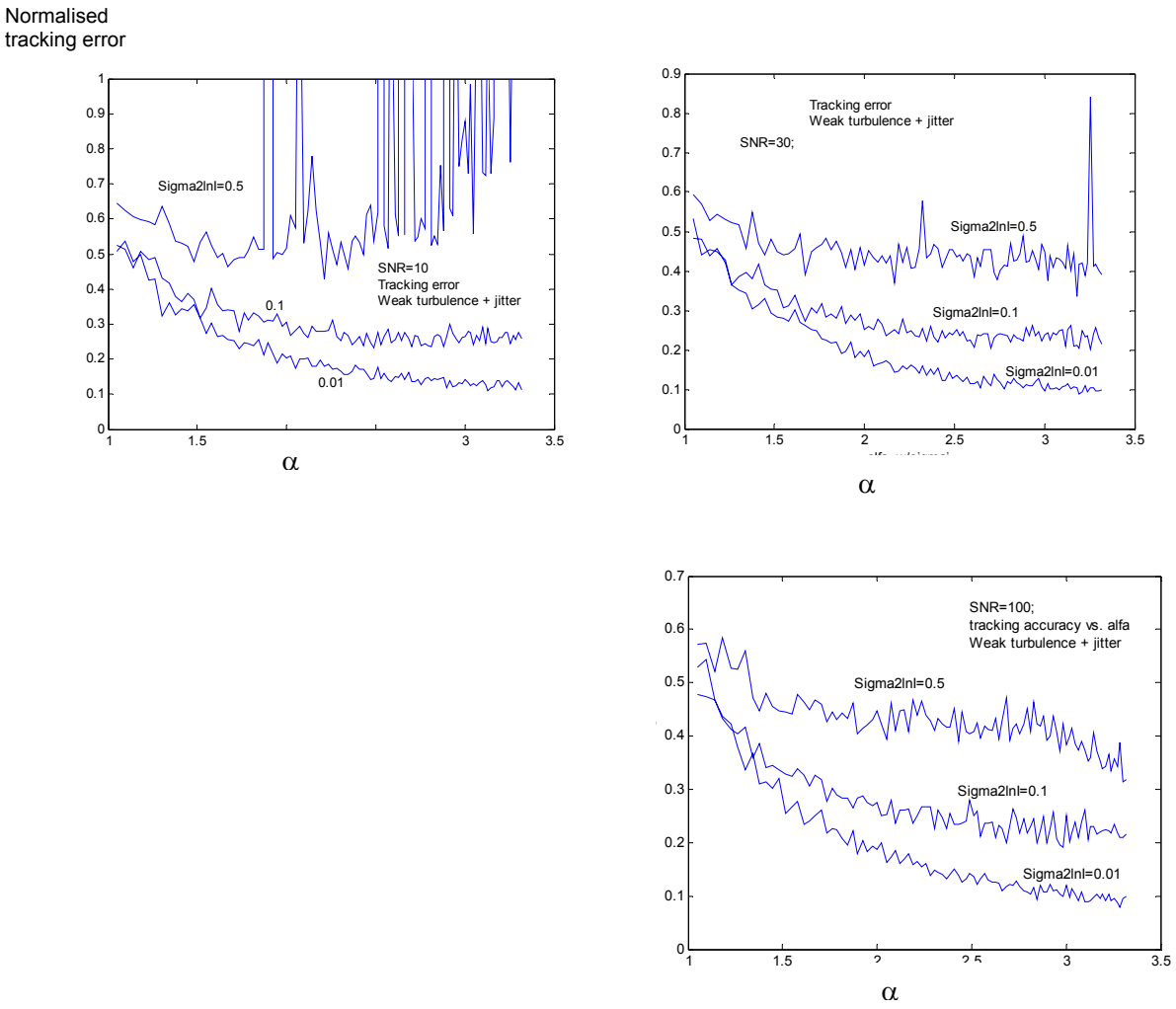

Figure 47. Normalised tracking error vs. α. Different nominal SNR (without jitter) are given in the figure. Weak turbulence and jitter.

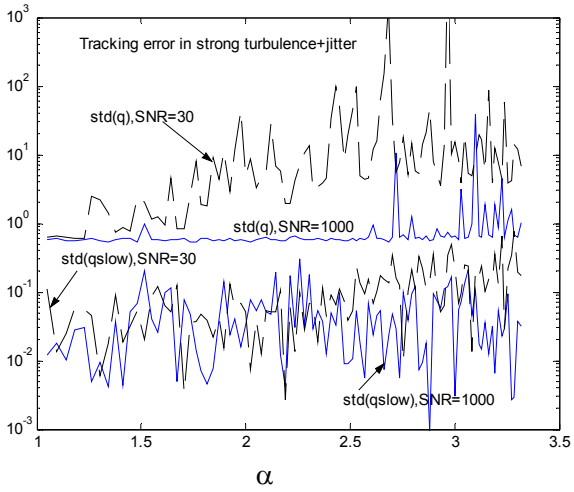

Figure 48. Normalised tracking error vs. α. Different nominal SNR (without jitter) are given in the figure. Strong turbulence and jitter.

8. REFERENCES

[1] Infrared Electro-Optical Handbook, vol. 2, SPIE Press, Bellingham, 1993.

[2] See e.g by L.C. Andrews and R.L. Phillips, "Laser Beam Propagation trough Random Media", SPIE Press, Bellingham, 1998.

[3] V.V. Vorobev, V.M. Osipov, V.S. Sirazetdinov, T.A. Sheremeteva, G.N. Filippov and D.G. Titterton, "Simulation of the propagation of a laser beam through local zone of strong turbulence", *J. Opt. Technol*., vol. 66, pp. 974-978, 1999.

[4] R.L. Fante, "Electromagnetic beam propagation in turbulent media", *Proc. IEEE*, vol. 63, pp. 1669-1692, 1975.

[5] R.L. Fante, "Electromagnetic beam propagation in turbulent media: An update", *Proc. IEEE*, vol. 68, pp. 1424-1443, 1980.

[6] J. H. Churnside and R. J. Lataitis, "Wander of an optical beam in the turbulent atmosphere", *Appl. Optics*, vol. 29, pp. 926-930, 1990.

[7] V.I. Klyatskin and A.I. Kon, "On the displacement of spatially-bounded light beams in a turbulent medium in the Markovian-random-process approximation", *Radiophys. Quant. Electr*., vol. 15, pp. 1056-1061, 1972.

[8] V.S. Sirazetdinov, D.I. Dmitriev, I.V. Ivanova and D.H. Titterton, "Effect of turbo-engine jet on laser radiation. Part1. Angular spectrum of disturbed beam", *Atmos. Ocean. Opt*., vol. 14, pp. 824-829, 2001.

[9] V.S. Sirazetdinov, D.I. Dmitriev, I.V. Ivanova and D.H. Titterton, "Effect of turbo-engine jet on laser radiation. Part2. Random wandering of disturbed beam", *Atmos. Ocean. Opt*., vol. 14, pp. 830-834, 2001.

[10] V.P. Kandidiv, M.P. Tamarov and S.A. Shlenov, "Spatial statistics of laser beams under conditions of small-scale turbulence simulations", *Atmos. Oceanic Opt*., vol. 9,pp. 916-920, 1996.

[11] V.P. Kandidov, M.P. Tamorov and S.A. Shlyonov, "Influence of the atmospheric turbulence outer scale on the variance of laser beam gravity center shifts", *Atmos. Oceanic Opt*., vol. 11, pp. 23-29, 1998.

[12] V.V. Vorob'ev, V.M. Osipov, V.S. Sirazetdinov, A.D. Starikov, T.A. Sheremet'eva, G.N. Filippov and D.G. Titterton, "Simulation of the propgation of a laser beam through local zones of strong turbulence", *J. opt. Technol*. Vol. 66, pp. 974-978, 1999.

[13] GLAD ver. 4.7, "General Laser Analysis Design", GLAD Theoretical manual ver. 4.7, AOR Inc., 2001.

[14] L.C. Andrews, R.L. Phillips and C.Y. Hopen, *Laser Beam Scintillation with Applications*, SPIE Press, Bellingham, 2001.

[15] L. Sjöqvist, S. Hård, B. Noharet and P. Rudquist, ”Retroreflective free-space optical communication – System analysis and performance”, FOI Report, FOI-R--0344--SE, 2001.

[16] K.G. Gilbert and L. J. Otten (Eds.), “Aero-optical phenomena”, vol. 80, *Progress in Astronautics and Aeronautics*, AIAA, New York, 1982.

[17] K. G. Gilbert, L. J. Otten and W. R. Rose, “Aerodynamic effects“, in *The infrared and electro-optical handbook*, vol. 2, SPIE Press, Bellingham, 1995.

[18] E.J. Jumper and E. J. Fitzgerald, “Recent advances in aero-optical phenomena”, *Progress in Aerospace Sciences*, vol. 37, pp. 299-339, 2001.

[19] V. N. Mahajan, “Strehl ratio for primary aberrations in terms of their aberration variance”, *JOSA Lett*., vol. 73, pp. 860-861, 1983.

[20] L. J. Otten and K. G. Gilbert, “Inviscid flow field effects: experimental results”, in *Aero-Optical Phenomena*, Eds. K. G. Gilbert and L. J. Otten, Vol. 80, Prog. in Astronautics and Aeronautics, AIAA, New York, 1984.

[21] A. E. Fuchs and S. E. Fuchs, “Optical Phase Distortion due to Compressive Flow over Laser Turrets”, in *Aero-Optical Phenomena*, Eds. K. G. Gilbert and L. J. Otten, Vol. 80, Prog. in Astronautics and Aeronautics, AIAA, New York, 1984.

[22] K.G. Gilbert, L.J. Otten and W.C. Rose, “Aerodynamic effects”, in *The Infrared & Electro-Optical Systems Handbook*, vol. 2, Atmospheric Propagation of Radiation”, Ed. F.G. Smith, SPIE Press, Bellingham, 1993.

[23] K. G. Gilbert and L. J. Otten (eds.), *Aero-Optical Phenomena*, Vol. 80, Prog. in Astronautics and Aeronautics, AIAA, New York, 1984.

[24] J.E. Craig and C. Allen, ”Aero-optical turbulent boundary layer/shear experiment on the KC-135 aircraft”, *Opt. Eng*., vol. 24, pp. 446-454, 1985.

[25] K. G. Gilbert, “LEAR Jet boundary layer/shear layer laser propagation measurements”, in *Aero-Optical Phenomena*, Eds. K. G. Gilbert and L. J. Otten, Vol. 80, Prog. in Astronautics and Aeronautics, AIAA, New York, 1984.

[26] K. G. Gilbert, “KC-135 Aero-optical turbulent boundary/shear layer experiments”, in *Aero-Optical Phenomena*, Eds. K. G. Gilbert and L. J. Otten, Vol. 80, p.306, Prog. in Astronautics and Aeronautics, AIAA, New York, 1984.

[27] O. Pade, “Models of turbulence for aero-optics application”, *Proc. SPIE*, vol. 4419, pp. 494-498, 2001.

[28] M. I. Jones and E. E. Bender, “CFD-based computer simulation of optical turbulence through aircraft flowfields and wakes”, *Proc. AIAA*, paper 2001-2798, 2001.

[29] I. Renhorn, “Mätnintg av optisk turbulens i jetflamma”, In Swedish, FOA Report, CH 30311-8.3,8.1, 1992.

[30] C. B. Hogge and W. L. Visinsky, “Laser Beam Probing of Jet Exhaust Turbulence”, *Appl. Optics*, vol. 10, pp. 889-892, 1971.

[31] J. L. Barett and P. A. Budni, “Laser beam propagation through strong turbulence”, *J. Appl. Phys*., vol. 71, pp. 1124-1127, 1992.

[32] Y.N. Evchenko et al., ”Spatial characteristic of laser radiation perturbed by a turbulent air flow”, *J. Opt. Technol*., vol. 65, p. 1039, 1998.

[33] V. S. Sirazetdinov et al., “Experimental Study of the Structure of Laser Beams Disturbed by Turbulent Stream of Aircraft Engine”, *Proc. SPIE*, vol. 3927, p.397, 2000.

[34] D. Titterton, “Measurements of the Distortion Generated in a Laser Beam’s Characteristics Resulting from Passage through an Engine’s Wake”, *RTO SET Symp., RTO MP-1*, p. 42-1, 1998

[35] V. V. Vorobev et al., ”Simulation of the propagation of a laser beam through a local zone of strong turbulence”, *J. Opt. Technol*., vol. 66, p. 974, 1999

[36] Sirazetdinov et al., “Study of Laser Beam Propagation through a Jet Aircraft Engine’s Exhaust“, *Proc. SPIE*, vol. 4167, p.120, 2001.

[37] O. Gustavsson, ”Laser guidance in light of high velocity missiles”, Presented at the SMi conference “Battlefield Lasers and Laser Countermeasures”, Hatton, London, 1999.

[38] S. Walles, ”Laser beam propagation through rocket plumes”, Lecture notes, Seminar given at FOI, 2000.

[39] C. J. Chen and W. Rodi, *Vertical Turbulent Buoyant Jets – A Review of Experimental Dat*a, Pergamon Press, Oxford, UK, 1980.

[40] M.A. Al-Habash, L.C. Andrews and R.L. Philips, “Double pass fade statistics of a laser beam under moderate to strong atmospheric turbulence”, *Proc. of the SPIE,* vol. 4272, Free-Space Laser Communication technologies XIII, 2001.

[41] M. Elbaum, P. Diament and W. Edelsson, ”Maximum angular accuracy of pulsed laser radar in photocounting limit,” *Appl. Optics*, vol. 16, No. 7, July 1977.